RSC Advances

PAPER

View Article Online
View Journal | View Issue

Cite this: *RSC Adv.*, 2022, **12**, 6888

Blue-red emitting materials based on a pyrido[2,3-*b*]pyrazine backbone: design and tuning of the photophysical, aggregation-induced emission, electrochemical and theoretical properties†

Deepak M. Kapse,[a] Pooja S. Singh,[a] Mohammed Ghadiyali,[b] Sajeev Chacko[b] and Rajesh M. Kamble *[a]

Received 8th January 2022
Accepted 12th February 2022

DOI: 10.1039/d2ra00128d

rsc.li/rsc-advances

Pyrido[2,3-*b*]pyrazine-based donor–acceptor–donor (D–A–D) molecules were designed by altering donor amines and synthesized using the Buchwald–Hartwig C–N coupling reaction. Further, the tunable opto-electrochemical properties of the dyes were studied in detail. The dye possesses intramolecular charge transfer (ICT) transition (412–485 nm), which marked the D–A architecture and induces a broad range of emissions from blue to red (486–624 nm) in the solution and solid state. Some of the dyes show aggregation-induced emission (AIE) features and formation of nanoparticles in the THF/H_2O mixture, as confirmed by DLS and FEG-SEM (of **7**) analysis. The AIE characteristics indicate its solid/aggregate-state application in organic electronics. The molecules exhibit high thermal stability, low band gap (1.67–2.36 eV) and comparable HOMO (−5.34 to −5.97 eV) and LUMO (−3.61 to −3.70 eV) energy levels with those of reported ambipolar materials. The relationship between the geometrical structure and optoelectronic properties of the dyes, as well as their twisted molecular conformation and small singlet and triplet excitation energy difference (ΔE_{ST} = 0.01–0.23 eV) were analyzed using the DFT/TDDFT method. Thus, potential applications of the dyes are proposed for optoelectronic devices.

Introduction

The relationship between the structure and opto-electrochemical properties of small donor–acceptor (D–A) molecules has been heavily investigated in the recent past.[1] Compared to polymeric materials, small D–A molecules have higher solubility in organic solvents, a defined molecular structure, and can be easily purified with reliable reproducibility. Additionally, these small D–A molecules possess intramolecular charge transfer (ICT) properties that can be exploited for tuning emission and electrochemical characteristics.[1]

The only major drawback is the aggregation-caused quenching (ACQ) phenomenon observed in planar D–A molecules as it causes quenching of emission hindering its application in organic light-emitting diodes (OLEDs).[2] However, ACQ can be overcome by simply having non-planar/twisted D–A molecules; here, the aggregation-induced emission (AIE) takes precedence through the assistance of restricted intramolecular rotation (RIR) and changes in the conformation of molecules in the aggregate state.[2] Further, twisted D–A systems can have adequately separated highest occupied (HOMO) and lowest unoccupied (LUMO) molecular orbitals with small energy gaps (ΔE_{ST}) between the singlet (S_1) and triplet (T_1) states. This indicates an efficient reverse intersystem crossing (RISC) process for the upconversion of $T_1 \rightarrow S_1$ excitons, possessing competent thermally activated delayed fluorescence (TADF) properties.[3]

Further, there is a scarcity of environmentally stable ambipolar materials, *i.e.* materials exhibiting electron and hole transport within the same molecule. This property enhances the power efficiency of devices, signifying the need for its development.[4] A known route for its development is by introducing electron-withdrawing groups (perfluorinated alkyl chains, cyano and carbonyl) or a more electronegative atom than carbon in an extended p-type material.[5]

From the literature, D–A molecules with acceptors such as quinoxaline,[6] indolo-quinoxaline,[7] pyrido[2,3-*b*]pyrazine,[8] and phenazine[9] are well known, due to their excellent semiconducting and highly emissive properties with outstanding AIE and TADF characteristics. Here, the pyrido[2,3-*b*]pyrazine acceptor is notable for its high electron-accepting ability, due to

[a]*Department of Chemistry, University of Mumbai, Santacruz (E), Mumbai 400 098, India. E-mail: kamblerm@chem.mu.ac.in*

[b]*Department of Physics, University of Mumbai, Santacruz (E), Mumbai 400 098, India*

† Electronic supplementary information (ESI) available: ^1H, ^{13}C, FT-IR and MALDI-TOF spectra of **1–10**; UV-visible absorption and emission spectra of **1** and **2–10** in other solvents, AIE spectrum and DLS plot; cyclic voltammogram, DFT/TDDFT calculation data along with molecular orbital diagram, optimized structure and computed geometrical parameters at S_0, S_1 and T_1 state are available. See DOI: 10.1039/d2ra00128d

its additional pyridine N-atoms in the fused ring mimicking quinoxaline. Hence, it is used for the fabrication of electroconductive and ambipolar electroluminescent devices,[8] while donors such as tri/diarylamines, carbazole, phenothiazine, and phenoxazine are generally used in the D–A system, as they help to tune optoelectronic properties, offering high conductivity and thermal stability.[3d,10]

In this work, we designed and synthesized D–A–D structured dyes **2–10** having pyrido[2,3-*b*]pyrazine acceptor and various diarylamines/heterocyclic amine donor groups. The standard Buchwald–Hartwig coupling amination reaction[11] is used for the synthesis and dyes have been characterized using spectroscopic techniques. The study presented here encompasses, tuning photophysical, aggregation-induced emission and electrochemical properties by modulating donor groups. Then, DFT and TDDFT techniques are used to understand the correlation between structure and properties; and the determination of ΔE_{ST}. The structures of dyes **2–10** are shown in Fig. 1.

Results and discussion

Synthesis and characterization

Molecule **1**, was synthesized by condensing 4,4′-dibromobenzil and 5-bromo-2,3-diaminopyridine in glacial acetic acid. For dyes **2–10**, the Buchwald–Hartwig coupling amination reaction[11] was employed to couple electron-donating diarylamines/heterocyclic amines at 4, 4′ and 7th position of molecule **1**. Products were purified by column chromatography using eluent *n*-hexane : chloroform with a yield of 41–97% as yellow-red solids. The identity and purity of products were confirmed by ^{1}H, ^{13}C NMR spectroscopy (ESI Fig. S30–S39†), FT-IR (ESI Fig. S25–S29†), MALDI-TOF mass spectrometry (ESI Fig. S20–S24†) and elemental analysis. The detailed synthesis route is shown in Scheme 1 and spectral characterization data is depicted in the experimental section.

Photophysical properties

The study of the charge transfer transition and fluorescence properties of dyes **2–10** in the solid film and different polarity of solvents; toluene, tetrahydrofuran (THF), chloroform (CHL), dichloromethane (DCM), and dimethyl sulfoxide (DMSO) was conducted using UV-visible and fluorescence spectroscopy techniques. Absorption spectra of dyes **2–10** in toluene and solid films are given in Fig. 2 (for other solvents ESI Fig. S4†). Emission spectra in toluene, DCM and solid films are given in Fig. 3(a, b) and 6(a) (for other solvents ESI Fig. S5†). The relevant noteworthy photophysical data are summarized in Tables 1 and 2.

Absorption property of dyes in solvent and solid state

UV-visible absorption spectra of molecule 1 in various solvent show absorption at 358–365 nm ($\log \varepsilon_{max}$ = 4.32–4.43 M^{-1} cm^{-1}) corresponding to n–π* and π–π* transitions originating from the π–conjugated pyrido[2,3-*b*]pyrazine skeleton (Fig. S1† and Table 1). Such transitions in dyes **2–10** were observed around 280–399 nm ($\log \varepsilon_{max}$ = 4.38–4.88 M^{-1} cm^{-1}). While additional transitions around 412–476 nm ($\log \varepsilon_{max}$ = 3.49–4.83 M^{-1} cm^{-1}) represent intra-molecular charge transfer

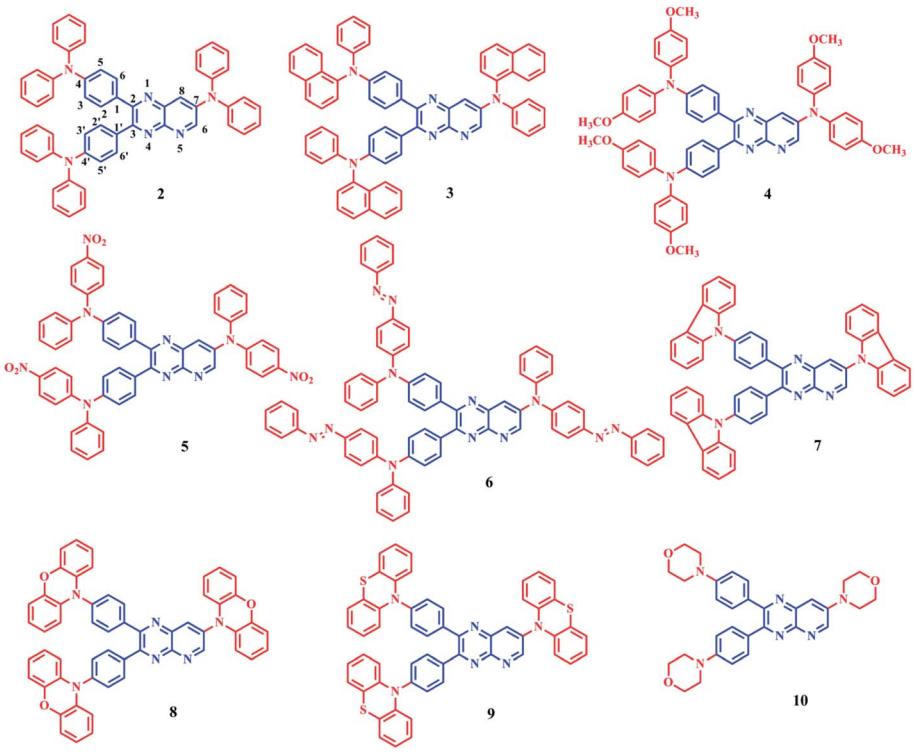

Fig. 1 Molecular structure of compounds **2–10**.

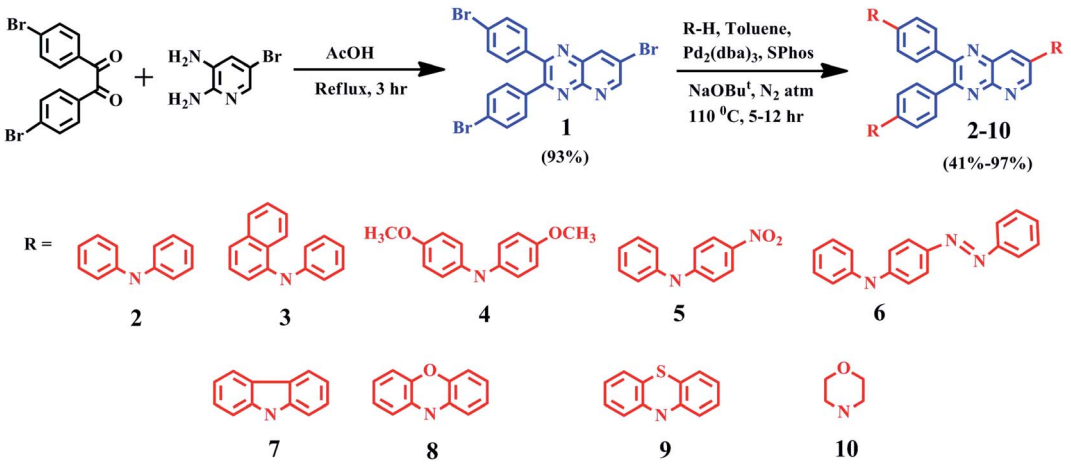

Scheme 1 Synthetic route of **2–10**.

(ICT) (Table 1). ICT establishes the D–A architecture in dyes **2–10**, originating from electron donor peripheral amines to the acceptor pyrido[2,3-*b*]pyrazine backbone (Fig. 2(a) and S4†).

Further, the ICT absorption wavelength of dyes **2–10** is sensitive towards the solvent polarity and the relative strength of the coupled donor amines, assisting tuning of ICT wavelength (Table 1). The marginal red shift of 5–6 nm and hypochromically shifted ICT maxima in dye **4** is the result of improved donating capacity due to the presence of a strong electron-donating methoxy ($-OCH_3$) group on diphenylamine, compared to **2** (Table 1, Fig. 2(a) and ESI Fig. S4†). Intense ICT transitions of **5** and **6** were ascribed to the electron-withdrawing nature of nitro ($-NO_2$) and phenyldiazene (–N=N–Ph) segments on diphenylamine, enabling charge-transfer contributions towards **5** and **6** from diphenylamine.[7b] Further, negative inductive (−I) and resonating (−R/−M) nature of the $-NO_2$ group in **5** decreases the electron density at the tertiary nitrogen atom of the amine by withdrawing the electron towards itself and leads to blue-shifted (17–20 nm) ICT maxima compared to **2** (Table 1, Fig. 2(a) and ESI Fig. S4†).[7b]

Weak donating strength of carbazole (CBZ) in dye **7** by its rigid/locked conformation leads to blue shift in ICT maxima (λ_{ICT} = 412–430 nm) compared to **2** (λ_{ICT} = 457–470 nm) (Table 1, Fig. 2(a) and ESI Fig. S4†).[8d,12] The oxygen and sulphur heteroatoms in rigid phenoxazine and phenothiazine offer the good electron-donating ability, leading to broader and stronger ICT as expected in dyes **8** and **9** in comparison to **7** (Fig. 2(a) and ESI Fig. S4†).[3e,6b,7b,8d,13] Observed behavior indicates a greater extent of separation in HOMO–LUMO spatial distributions compared to other dyes, which is evaluated by the theoretical data (ESI Fig. S54 (below), S55 (above)†).[3e,6b,7b,8d,13] Weak donor strength of aliphatic cyclic amine (morpholine) in **10** leads to blue-shifted ICT band compared to **2** (Fig. 2(a) and ESI Fig. S4†). While slightly broader and red-shifted solid film absorption maxima were found it suggested molecular aggregation in the solid-state (Table 1 and Fig. 2(b)).[14]

Emission property of dyes in the solvent state

Photoexcitation of molecule **1** (at absorption λ_{max}) shows an unstructured emission (ESI Fig. S2 and S3†), while dyes **2–10** (on respective ICT λ_{max}) display emission between blue to yellow (λ = 486–585 nm) in the solution state (Table 2, Fig. 3, ESI Fig. S5†). The absence of vibrionic structure in emission spectra of **2–10** recommends emission from relaxed ICT state.[15] Analogous to absorption, the emission wavelength was also tuned by the modification of the amine segment in **2–10** (Table 2, Fig. 3,

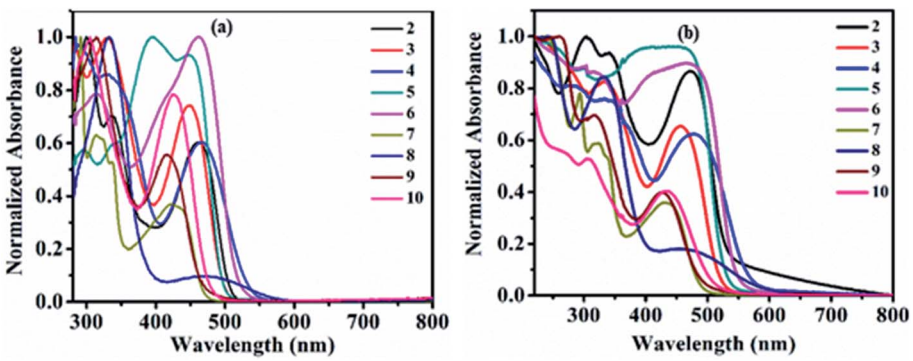

Fig. 2 UV-Vis absorption spectra of compounds **2–10** in toluene (a) and solid film (b).

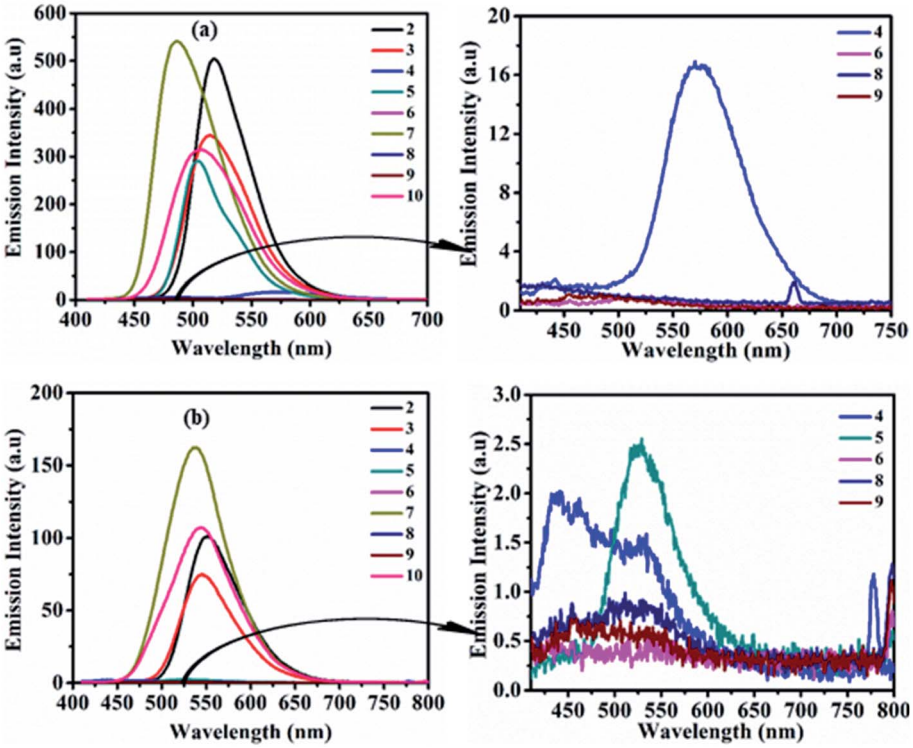

Fig. 3 Emission spectra of **2–10** (left) and of weak/non-emissive molecules (right) in toluene (a) and DCM (b) (excitation of molecules **2–10** done at their respective ICT λ_{max}).

ESI Fig. S5†). Molecule **4** having strong donating $-OCH_3$ or polar substituent show weak emission with bathochromic shift in nonpolar toluene and moderately polar THF solvent, compared to **2**. While, due to the enhancement in the electron density on the tertiary nitrogen atom of diphenylamine by the electron-donating/polar $-OCH_3$ group in **4**, it restricts the rotation of the phenyl group in polar media. Hence, its emission in highly polar CHL, DCM and DMSO solvents was found almost quenched due to polar–polar solute–solvent interactions.[15,16]

In the case of **5**, strong CT character and –I/−R/−M nature of the $-NO_2$ group on the donor amine contributes hypo and hypsochromically-shifted emission compared to **2** in nonpolar toluene and afterwards emission intensity goes on decreasing on increasing the polarity of the solvent from THF to DMSO.

Table 1 Absorption data of molecules **1–10**

	$\lambda_{abs}{}^{a,b}$, nm (log ε_{max} M^{-1} cm^{-1})					λ_{abs}, nm
Dye	Toluene	THF	Chloroform	DCM	DMSO	Solid film
1	362 (4.37)	358 (4.32)	365 (4.43)	363 (4.40)	361 (4.38)	368
2	300 (4.66), 335 (4.50), 462 (4.44)	297 (4.61), 337 (4.49), 457 (4.44)	301 (4.72), 338 (4.60), 470 (4.51)	299 (4.69), 337 (4.55), 464 (4.46)	299 (4.70), 336 (4.58), 465 (4.44)	304, 341, 476
3	329 (4.53), 449 (4.40)	333 (4.49), 447 (4.39)	330 (4.65), 458 (4.49)	327 (4.56), 453 (4.41)	328 (4.60), 452 (4.43)	334, 462
4	284 (4.64), 329 (4.56), 465 (4.42)	281 (4.68), 331 (4.58), 462 (4.40)	325 (4.58), 476 (4.39)	282 (4.70), 329 (4.57), 467 (4.42)	280 (4.66), 331 (4.57), 464 (4.36)	290, 340, 479
5	296 (4.49), 398 (4.73), 450 (4.70)	294 (4.42), 399 (4.79), 440 (4.70)	299 (4.50), 451(4.82)	297 (4.50), 446 (4.82)	298 (4.50), 440 (4.83)	300, 464
6	313 (4.58), 461 (4.68)	312 (4.51), 458 (4.68)	317 (4.69), 472 (4.79)	312 (4.64), 460 (4.73)	311 (4.64), 462 (4.72)	304, 475
7	291 (4.80), 314 (4.60), 423 (4.37)	291 (4.81), 337 (4.44), 420 (4.33)	291 (4.82), 320 (4.66), 430 (4.41)	291 (4.85), 313 (4.65), 423 (4.41)	292 (4.88), 320 (4.65), 412 (4.34)	294, 322, 437
8	333 (4.57), 467 (3.53)	333 (4.54), 466 (3.49)	335 (4.65), 472 (3.65)	332 (4.60), 464 (3.52)	332 (4.66), 469 (3.56)	333, 485
9	314 (4.43), 417 (4.17)	312 (4.38), 416 (4.14)	313 (4.57), 424 (4.32)	313 (4.48), 419 (4.23)	315 (4.47), 416 (4.12)	317, 428
10	305 (4.42), 426 (4.31)	358 (4.44), 420 (4.23)	305 (4.47), 428 (4.37)	306 (4.44), 428 (4.33)	308 (4.50), 433 (4.36)	304, 440

[a] Recorded in 10^{-5} M solution. [b] ε is extinction coefficient (L mol^{-1} cm^{-1}) (in parentheses).

Table 2 Emission data, optical band gap, Stoke's shift and quantum yield of **2–10** in the solution state

	λ_{emi}[a] nm, (E_g^{opt} eV)[b]					Stoke's shift[c], cm^{-1} (% ϕ_F)[d]				
Dye	Toluene	THF	Chloroform	DCM	DMSO	Toluene	THF	Chloroform	DCM	DMSO
2	520 (2.41)	530 (2.40)	550 (2.33)	552 (2.32)	**558** (2.31)	2414 (12.73%)	2906 (11.30%)	2959 (6.36%)	3435 (3.64%)	**3584 (0.14%)**
3	515 (2.46)	526 (2.44)	546 (2.38)	547 (2.37)	**553** (2.37)	2854 (9.09%)	3177 (11.11%)	3519 (4.72%)	3793 (2.36%)	**4040 (0.19%)**
4	**570** (2.30)	**585** (2.26)	NA (2.19)	NA (2.24)	NA (2.24)	**3961 (0.71%)**	**4551 (0.11%)**	NA	NA	NA
5	503 (2.52)	526 (2.52)	**529** (2.49)	**531** (2.49)	NA (2.49)	2390 (16.36%)	3496 (0.55%)	**3517 (0.14%)**	**3792 (0.04%)**	NA
6	NA (2.38)	**507** (2.38)	**537** (2.35)	NA (2.34)	NA (2.31)	NA	**2226 (0.06%)**	**2654 (0.16%)**	NA	NA
7	486 (2.60)	519 (2.55)	530 (2.52)	538 (2.52)	**555** (2.51)	3064 (18.18%)	4094 (13.33%)	4387 (9.09%)	5053 (5.45%)	**6253 (0.34%)**
8	NA (2.14)	NA (2.13)	NA (2.10)	NA (2.10)	NA (2.07)	NA	NA	NA	NA	NA
9	NA (2.64)	NA (2.48)	NA (2.45)	NA (2.44)	NA (2.42)	NA	NA	NA	NA	NA
10	508 (2.52)	534 (2.52)	540 (2.45)	542 (2.45)	**543** (2.44)	3955 (13.63%)	4429 (6.85%)	4845 (5.45%)	4914 (4.91%)	**4678 (0.46%)**

[a] Recorded in 10^{-5} M solution. [b] Optical band gap estimated using offset wavelength derived from the low energy absorption band $\left(E_g^{opt} = \frac{1240}{\lambda_{abs.\ edge}}\right)$ eV. [c] Stoke's shift calculated according to the equation $\Delta\nu = (1/\lambda_{abs} - 1/\lambda_{em}) \times 10^7$ (cm^{-1}) [d] Percentage quantum yield (in parentheses) with reference to quinine sulfate (ϕ_F = 0.54 in 0.5 M H_2SO_4). NA: quenched emission, Bold: emission property (wavelength, Stoke's shift and quantum yield) of dyes having very low intensity.

The high sensitivity of this molecule (**5**) to solvent polarity is due to reverse charge shift from the amino group in the excited state to the $-NO_2$ substituent leading to an enhancement in excited state dipole moment, which interacts with the polar solvent molecules and reduces the energy of the excited state hence shows weak emission in polar solvents (Table 2, Fig. 3 and ESI Fig. S5†).[15] Moreover, molecule **6** shows faint emission in THF, CHL and quenched emission in rest other solvents, which could be due to *cis–trans* photoisomerization of azobenzene chromophores.[17]

Locked conformation of CBZ in **7** effects weak donating strength and a lesser degree of rotational freedom in solution state compared to diphenylamine in **2**, as a result, emission band was found blue shifted (3–34 nm) (Table 2, Fig. 3, ESI Fig. S5†).[8d,12,18] Further observed quenched emission in dyes **8** and **9** having phenoxazine and phenothiazine units were explained by (i) the photo-induced electron transfer (PET) process, which leads to the formation of collision complexes or exciplexes in the D–A assembly or (ii) inefficient electron delocalization of the heteroatoms in order to retain aromaticity of two benzo-fused rings of phenoxazine and phenothiazine units respectively.[19] Weak donating strength of aliphatic cyclic amine (morpholine) induces 12–15 nm blue-shifted emission maxima in **10** compared to **2** (Table 2 and Fig. 3, ESI Fig. S5†).

Stoke's shift of dyes is found high as 2226–6253 cm^{-1} (Table 2), suggesting a change in the ground and excited state geometry and no reabsorption of the emitted photons, which is desirable for their application in optoelectronics. The optical band gap (E_g^{opt}) of dyes were found in the range of 2.07–2.64 eV (Table 2). The quantum yield of compounds **2–10** (calculated using quinine sulfate (ϕ_F = 0.54 in 0.5 M H_2SO_4) as reference material) was found in the range of 0.04–18.18% in the solution state (Table 2). The variation in ϕ_F of dyes in different solvents depends on the change in the non-radiative decay rates or conformational change in the fluorophore as the excitation coefficient and radiative decay rates are independent of solvent polarity.[15] The obtained high ϕ_F in nonpolar solvents than in highly polar DMSO solvent could be due to stabilization of ICT state causing an increase in the non-radiative decay rate in the higher-polarity solvents.[15] Further observed low quantum efficiency could be due to an increase in non-radiative decay rate by the rotation of the amino group in dyes, which provides a rapid deactivation pathway to the ground state.[15]

Solvatochromic effect

The emission properties of dyes **2**, **3**, **5**, **7** and **10** are found to be sensitive toward the polarity of the solvent (Table 2 and Fig. 4). The solvatochromic effect on these dyes was assessed using the Reichardt polarity parameters E_T (30) and Reichardt–Dimroth

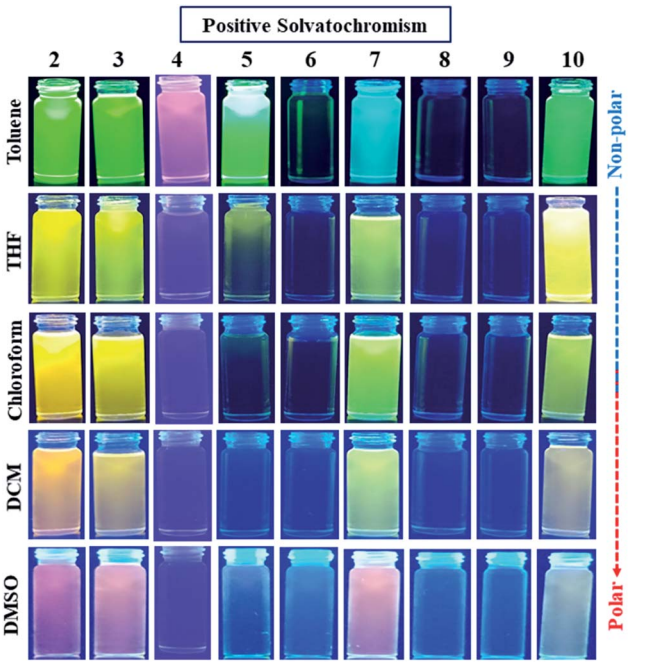

Fig. 4 Emission images of **2–10** showing a positive solvatochromic effect in varying polarity of solvents under UV (365 nm) lamp.

E_T^N,[20] Weller's $\left(\Delta f_w = \frac{\varepsilon-1}{2\varepsilon+1} - \frac{\eta^2-1}{4\eta^2+2}\right)$,[21] Rettig's $\left(\Delta f_R = \frac{\varepsilon-1}{\varepsilon+2} - \frac{\eta^2-1}{2\eta^2+4}\right)$,[22] Lorentz–Lorenz $\left(f(\eta^2) = \frac{\eta^2-1}{2\eta^2+1}\right)$, Kirkwood–Bauer–Magat $\left(f(\varepsilon) = \frac{\varepsilon-1}{2\varepsilon+1}\right)$, Lippert–Mataga $(f_{LM}(\varepsilon,\eta) = f(\varepsilon) - f(\eta^2))$[23] McRae $\left(f_{MR}(\varepsilon,\eta) = \frac{\varepsilon-1}{\varepsilon+2} - \frac{\eta^2-1}{\eta^2+1}\right)$[24] and Bakshiev's $\left(f_B(\varepsilon,\eta) = \frac{2\eta^2+1}{\eta^2+2}\left(\frac{\varepsilon-1}{\varepsilon+2} - \frac{\eta^2-1}{\eta^2+2}\right)\right)$[25] function plots (Fig. 5).

The bathochromic shift or good linear correlation of emission wavelength of dyes with increasing value of E_T (30) and E_T^N function of solvents suggests the existence of a positive solvatochromic effect in the dyes (Fig. 5(a and b)).[15,20] Herein, polar solvent solvate the excited state of charge transfer by stabilizing enhanced dipole moment of the excited state than the ground state and subsequently show red-shifted emission and decreases emission intensity with a reduction in the energy gap.[15,20]

A further possibility of occurrence of the TICT state in polar media and dependency of absorption and emission maxima on solvent polarity during charge transfer are accessed by a good linear correlation of emission wavelength of dyes with Weller and Rettig's functions (Fig. 5(c and d)).[21,22]

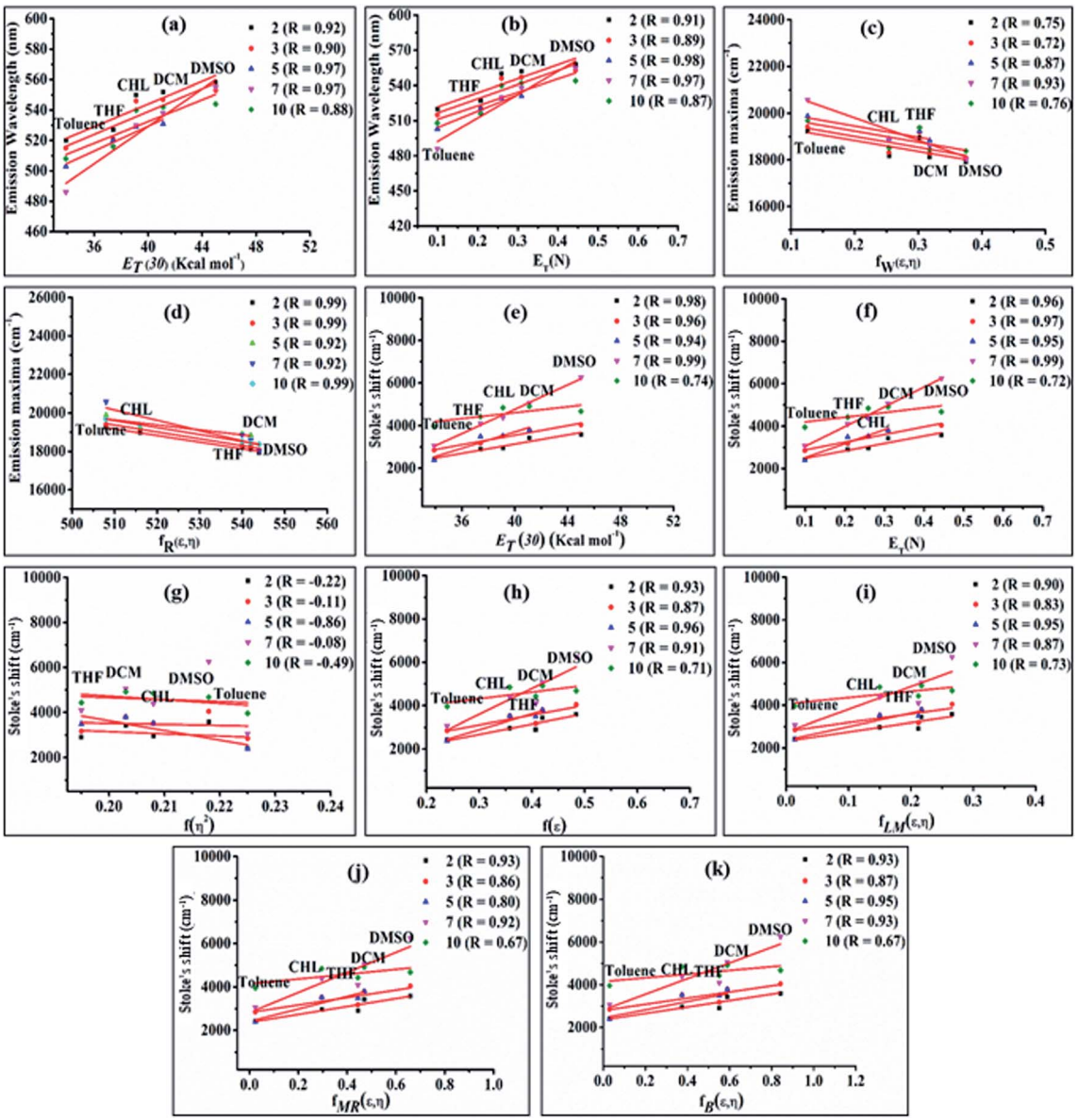

Fig. 5 Plot of emission wavelength (nm) *vs.* the Reichardt empirical solvent polarity parameter E_T(30) (a) and Reichardt–Dimroth function E_T^N (b); emission wavelength (cm^{-1}) *vs.* Wellers ($f_W(\varepsilon,\eta)$) (c) and Rettig's ($f_R(\varepsilon,\eta)$) (d) function; plot of Stoke's shift *vs.* Reichardt empirical solvent polarity index (E_T(30)) (e), Reichardt–Dimroth (E_T^N) (f), Lorentz–Lorenz ($f(\eta^2)$) (g), Kirkwood–Bauer–Magat ($f(\varepsilon)$) (h), Lippert–Mataga polarity ($f_{LM}(\varepsilon,\eta)$) (i), McRae ($f_{MR}(\varepsilon,\eta)$) (j) and Bakshiev's ($f_B(\varepsilon,\eta)$) (k) function of **2**, **3**, **5**, **7** and **10**.

Additionally, Stoke's shift of these dyes was found to vary linearly with the E_T^N and $E_T(30)$ gives evidence of the occurrence of positive solvatochromism (Fig. 5(e and f)).[15,20] The independence of solvents refractive index (η) in the determination of the ground and excited-state properties of the molecules are demonstrated by nonlinear solvent polarizability plots, *i.e.* plot of Stoke's shift of dyes *vs.* $f(\eta^2)$ of various solvents (Fig. 5(g)). Besides prominence of solvent dielectric polarizability on the ground and excited-state photophysical properties of molecules are revealed by a good linear correlation in the plot of Stoke's shift *vs.* $f(\varepsilon)$ or the solvent polarity plot (Fig. 5(h)).[15]

Additionally, the obtained good linear correlation in the Lippert–Mataga plot, *i.e.* the plot of Stoke's shift *vs.* $f_{LM}(\varepsilon,\eta)$ marked the presence of general solvent effect and the presence of positive solvatochromic behaviour with charge transfer characteristics in these dyes (Fig. 5(i)).[15,23] In addition, positive solvatochromism and CT characteristics were also established by the linearity of Stoke's shifts with improved Lippert–Mataga functions, *i.e.* McRae ($f_{MR}(\varepsilon,\eta)$) and Bakhshiev ($f_B(\varepsilon,\eta)$) functions (Fig. 5(j and k)).[15,24,25]

Emission property of dyes in the solid-state

As solid/aggregate state emission is desirable for practical application of D–A molecules. Herein dyes **2–10** (except **6**), emit at λ_{max} = 531–624 nm and cover green to red emission range in solid-state (Fig. 6). Dyes **2** (553 nm), **3** (551 nm), **5** (548 nm), and **7** (531 nm) shows good solid-state emission, while **4** (601 nm), **8** (624 nm), **9** (607 nm) and **10** (550 nm) are weakly emissive (Fig. 6). Whereas photoisomerization of azobenzene chromophore present in dyes **6** make it nonemissive in solid-state (Fig. 6).[17,26]

Optimized geometries and ground state geometrical parameters (dihedral angle) of dyes suggest all aromatic rings rotate to some degree between each other and hence attain non-planar/twisted spatial conformation at their lowest energy states (ESI Tables S11–S20, Fig. S41–S50†). However twisting patterns in molecules **2–10** vary in accordance with their variation in the dihedral angle between D and A units (ESI Tables S11–S20 and Fig. S41–S50†). Non-planar conformation of dyes prevents close packing and π–π interactions, resulting in more or less emission in the solid-state (Fig. 6).[18,27]

As literature manifests, solid-state emission is one of the main criteria for the existence of AIE properties.[2] Consequently, it is assumed that the good solid-state emissions of D–A–D pairs **2**, **3**, **5** and **7** may exhibit AIE properties. Thus, to evaluate and understand the aggregation-based emission enhancement/quenching phenomenon, we studied the AIE characteristics of dyes, as depicted in the following section.

Aggregation-induced emission

AIE characteristics of the dyes were analyzed by using a series of 10^{-5} M THF/water mixtures with varying (0–90) percentages of water fraction (f_w). Preliminary observation of changes in a series of THF/water mixture of dyes was done under visible and 365 nm UV illumination (Fig. 7(a–d), ESI Fig. S18†).

In the visible light, all dyes show formation aggregated homogenous suspension (except **10**) at high f_w due to the immiscibility of dyes in water. Homogeneous suspensions are with no precipitate of aggregates hence called nanoparticles (Fig. 7(a–d), ESI Fig. S18†).[2c] In addition under 365 nm UV illumination dyes **2**, **3**, **4**, **5** and **7** exhibit increased emission at aggregated or high f_w solution than the previously quenched

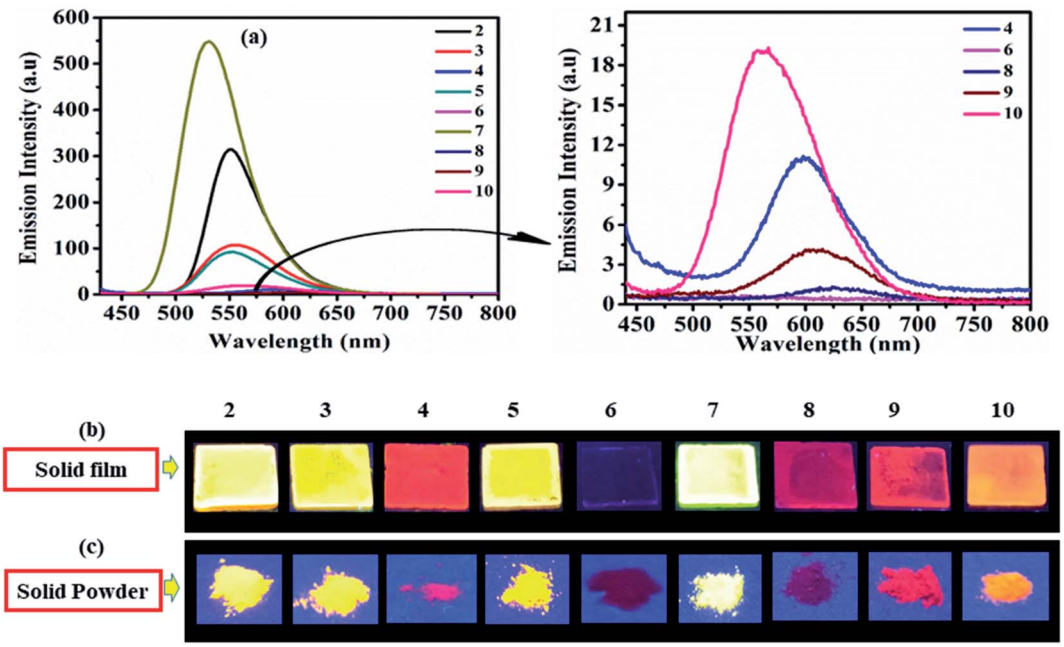

Fig. 6 Emission spectra of **2–10** (left) and of weak/non-emissive molecules (right) in solid film (a), emission images in solid film (b) and solid powder (c) of **2–10** under UV (365 nm) lamp.

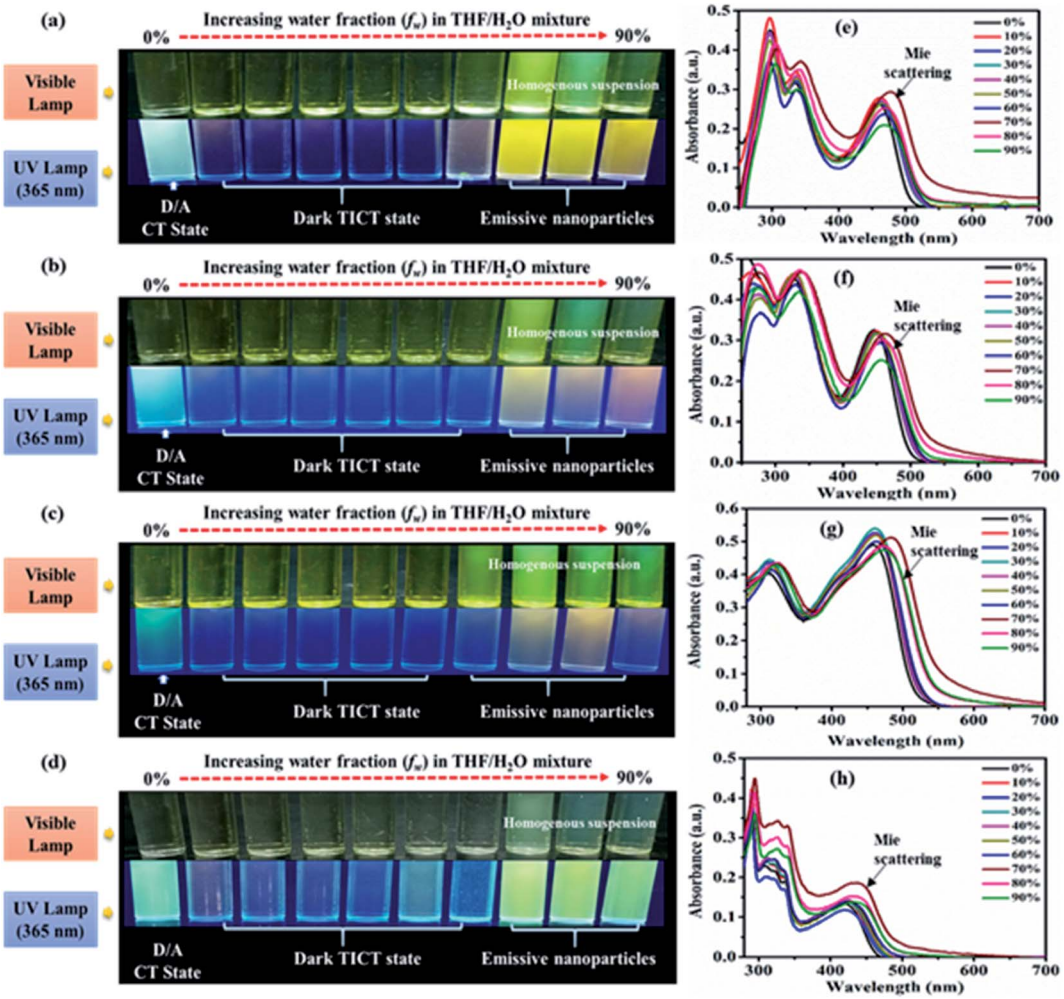

Fig. 7 Emission images of **2** (a), **3** (b), **5** (c) and **7** (d) and absorption spectra of **2** (e), **3** (f), **5** (g) and **7** (h) recorded in 10 μM solution of different THF-H_2O mixtures with increasing percentage of water fraction (f_w).

isolated (less f_w) media designated possibility of AIE phenomenon (Fig. 7(a–d), ESI Fig. S18(a)†). While in the case of **6**, **8**, **9** and **10** quenched emissions in an aggregate state marked AIE inactivity or ACQ effect of dyes (ESI Fig. S18(b–e)†). Furthermore, aggregation-based effects in the dyes **2–10** were evaluated using UV-Vis (Fig. 7(e and f), ESI Fig. S6†) and fluorescence spectroscopy (Fig. 8(a–d), ESI Fig. S7†).

UV-visible spectra of all the dyes at low f_w in THF/water mixtures reveal an identical CT λ_{max} with decreasing absorbance (Fig. 7(e and f), ESI Fig. S6†). While at high f_w (~60%/70%) showed an increase in the absorption intensity with extended wavelength or level-off tail characteristics in the visible spectral region (Fig. 7(e and f), ESI Fig. S6†). Such level-off tails are called "Mie-scattering" which are often associated with the formation of nanoparticles due to the hydrophobic environment created inside a mixture.[2,28] Also increased absorbance at high f_w specifies better conjugation in the nanoparticles as compared to their counterparts of isolated species.[2]

The emission in pure THF media of the dyes **2**, **3**, **5** and **7** are a result of CT transition (Fig. 8). The gradual addition of water (10–60%) into THF solutions of **2**, **3** and **7**, results in adversely quenched emission (Fig. 8(a, b, d, e, f and h)). This could be ascribed by: (i) the solvatochromic effect due to increased polarity inside the mixture (ii) conformation changes and the conversion of CT to TICT state, usually associated with non-radiative quenching process leading to 'dark state'.[2a–c,15] Further addition of high f_w (70%) creates a hydrophobic environment due to insolubility of dyes in water leading to the formation of emissive nanoparticles inside the THF/H_2O mixture (Fig. 8(a, b, d, e, f and h)). The formation of nanoparticles at 70% f_w considerably restricts the intramolecular rotation (RIR), which limits the ICT effect, blocks the non-radiative channel and boosts up the emission intensity in an aqueous mixture.[2,15] Hence entitles AIE effect in dyes **2**, **3** and **7**.

Also, nearly matching solid film emission wavelength with the aggregate emission formed at 70% f_w depicts the formation of emissive nanoparticles at higher water f_w and AIE activity.[2,15] However, the extent of AIE activity in **3** is comparatively weaker

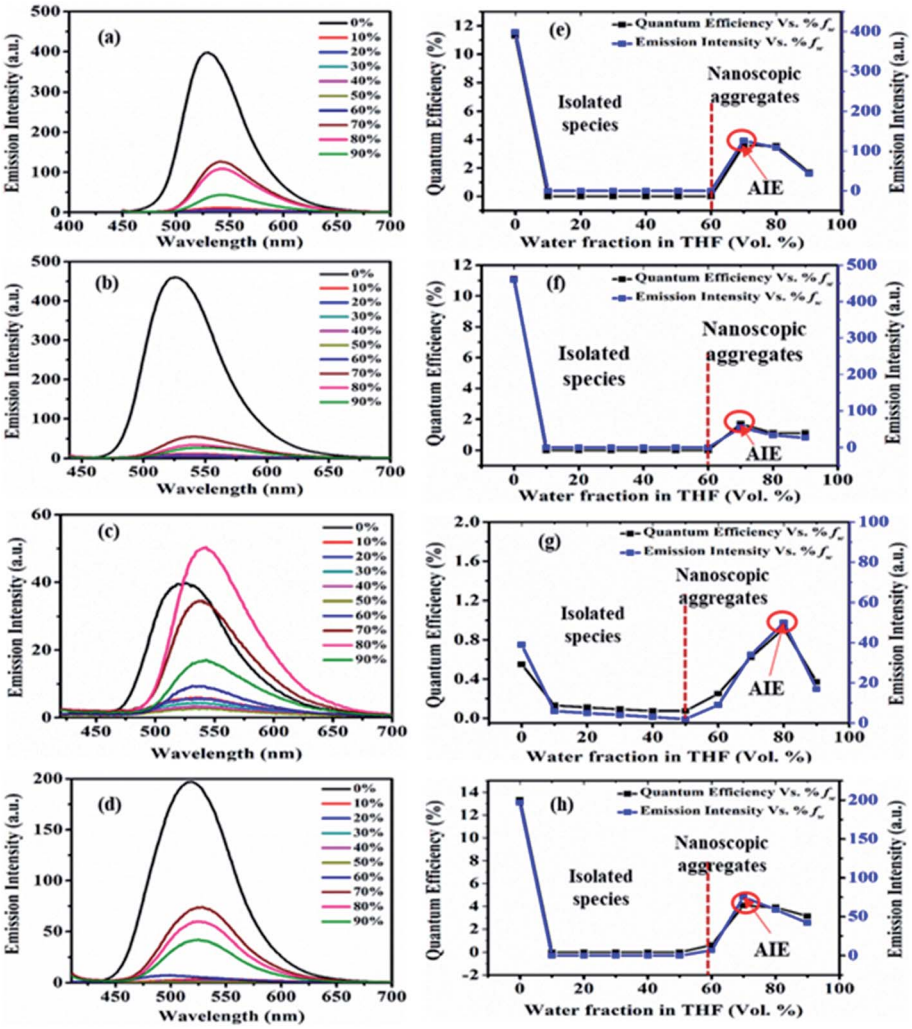

Fig. 8 Emission spectra of **2** (a), **3** (b), **5** (c) and **7** (d) recorded in 10 μM solution of THF–H_2O mixture with increasing percentage of water fraction (f_w). Plot of percentage quantum efficiency and emission intensity *vs.* percentage of water fractions (f_w) of **2** (e), **3** (f), **5** (g) and **7** (h) in the THF/water mixture.

than in **2** and **7**. Moreover, at 80% and 90% f_w decrease in emission could be due to different physical constraints of the molecules, changes in morphological structure, random molecular packing, and the variable size of particles formed in the aggregate state.[2a–c,15]

The presence of nanoparticles and their hydrodynamic average size in THF/H_2O homogeneous suspensions of dyes were confirmed by the dynamic light scattering (DLS) data (Fig. 9, ESI Fig. S9–S17†). The low polydispersity indices (PDI) (except **10**) obtained from DLS also confirmed the homogeneity of the homogeneous suspensions (Fig. 9, ESI Fig. S9–S17†). The hydrodynamic average size of nanoparticles formed in 70–90% f_w of the THF/H_2O mixture of the dyes **2** (132, 327, 328 nm), **3** (102, 165, 290 nm) and **7** (127, 156, 266 nm), suggested size-dependent emission behavior upon aggregation (Fig. 9(a, b and d), ESI Fig. S9, S10, S14†). Also, the FEG-SEM image of nanoparticles formed in 70% f_w of THF–H_2O mixture of **7** shows a circular morphology, with a mean diameter of about 24–35 nm (Fig. 10).

In the case of dye **5**, emissions get quenched with the addition of water from 10% to 50% f_w. Afterward, gradual enhancement in the emission with the addition of 60% to 80% f_w could be due to the hydrogen bond-assisted AIE effect in dye **5** (Fig. 8(c and g)).[2a–c,15] H-bonds between water molecules and $-NO_2$ group effectively stiffen the conformation of dye and contribute to the RIM processes leading to AIE activity.[2a–c,15] Similarly dye **4** also shows slight emission enhancement at 70–90% f_w compared to quenched emission at 10–60% f_w. However, the strength of emission was quite weak, designating a very feeble AIE effect (ESI Fig. S7(a), S8(a)†). Besides, similar to dyes **2**, **3** and **7**; a variation in the emission intensity with the size of nanoparticles formed in aggregated media of **4** (70–90% f_w are 131, 464, 662 nm) (ESI Fig. S11†) and **5** (60–90% f_w are 694, 164, 100, 204 nm) (Fig. 9(c) and ESI Fig. S12†) was observed. While dye **10** shows a subsequent decrease in emission with the gradual addition of water suggesting the ACQ phenomenon (ESI Fig. S7(e) and S8(b)†). Also observed higher PDI value at high f_w in THF solvent of **10**, attribute a very broad or multiple particle

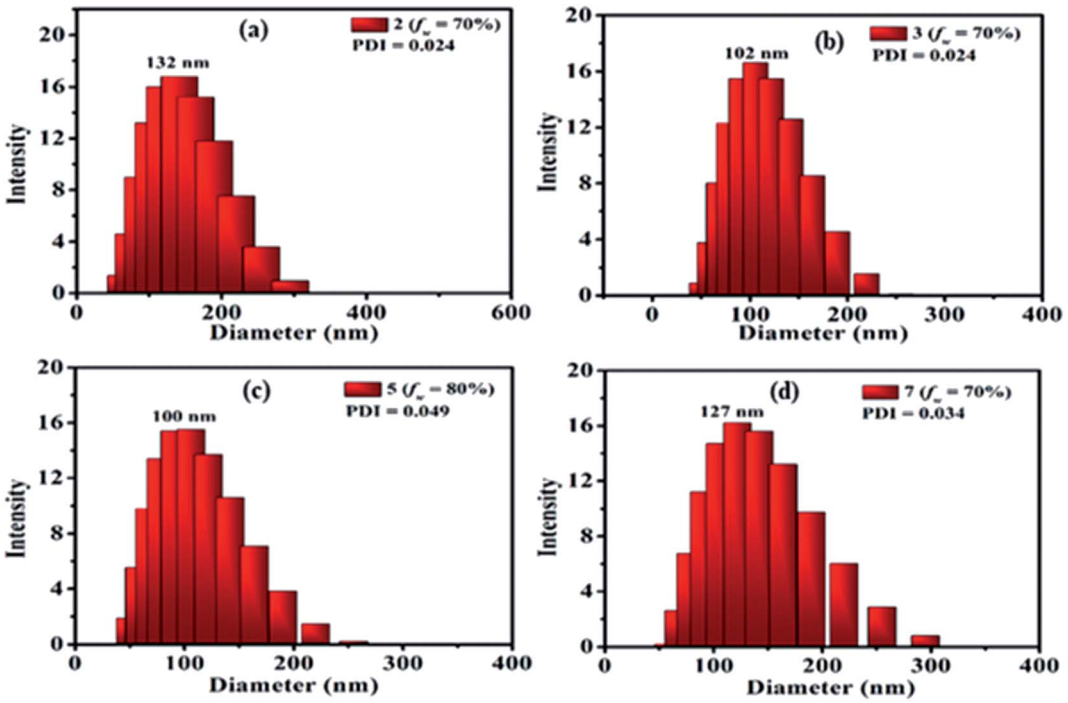

Fig. 9 DLS plots of **2** (a), **3** (b), **5** (c) and **7** (d) obtained from 70%/80% f_w of THF–H_2O suspension.

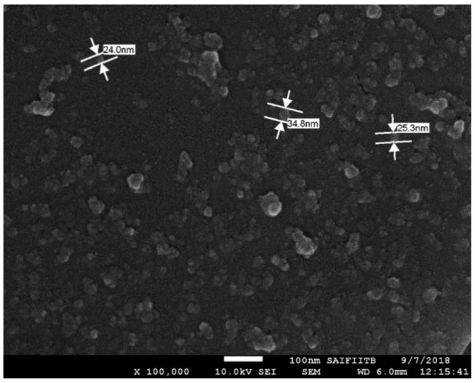

Fig. 10 FEG-SEM image of **7** obtained from 70% f_w of THF–H_2O suspension.

size distribution due to fast agglomeration of molecules in that media and hence evident the ACQ effect (Fig. S17†).[3d,29]

Furthermore, the quantum efficiency in **2**, **3** and **7** decreases from 10% to 60% f_w, after that, a rise in ϕ_F at 70% f_w designates the AIE effect (Fig. 8(e, f and h)). Similarly, the case of **4** (ESI Fig. S8(a)†) and **5** (Fig. 8(g)) shows a rise in quantum efficiency from 70–90% f_w and 60–90% f_w, compared to the values at low f_w suggesting the AIE effect. But the obtained very low ϕ_F at high f_w of dyes **4** and **5** compared to **2**, **3** and **7** further demonstrate a very weak AIE effect. While molecule **10** shows a decrease in ϕ_F at high water fraction proposing the ACQ phenomenon (ESI Fig. S8(b)†).

In the case of dye **6** nonemissive nature at the aggregate state and AIE inactivity could be due to the inability of the molecule to restrain photoisomerization of the azo (–N=N–) core at the aggregate state.[17,26] While AIE inactivity in molecules **8** and **9** could be justified by the covalent locking of donor phenyl ring by oxygen and sulphur, respectively. Here, the RIR process does not work in the aggregate state as its donor phenyl ring rotations are already locked by the "O/S" bridges, and hence its emission at high f_w is not enhanced and AIE inactivity for these dyes are observed.[2a,7b,30] While the formation of nanoparticles in a homogenous suspension (at high f_w) is evident by the presence of Mie-scattering in absorption spectra (ESI Fig. S6 (b–d)†) as well as from the hydrodynamic average size obtained from DLS data (SI Fig. S13, S15, S16†). The hydrodynamic average size of nanoparticles formed in 70–90% f_w of the THF/H_2O mixture for the dye **6** are 200, 206, 402 nm; for **8** are 128, 140, 215, 336 nm and for **9** are 135, 130, 218, 377 nm (ESI Fig. S13, S15, S16†). Thus, tuning of donor amines alters the aggregation-based AIE property in dyes **2–10.**

Electrochemical properties

The redox behavior and associated HOMO and LUMO energy levels of **1–10** were studied using cyclic voltammetry (CV). Redox behavior of **2** and **5** are shown in Fig. 11 (for other ESI Fig. 19†) and the relevant electrochemical data are presented in Table 3. Cyclic voltammogram of **1** shows no oxidation peak (ESI Fig. S19†), however, the C–N linkage in **2–10** induces oxidation potential and established strong D–A interaction. As a result, on the anodic sweep, three/two quasi-reversible waves in the range of 0.79–1.62 V are observed for **2–10** (Fig. 11, ESI Fig. 19 and Table 3†). This is attributed to the oxidation of diarylamine/heterocyclic amines coupled with pyrido[2,3-*b*]pyrazine moiety.

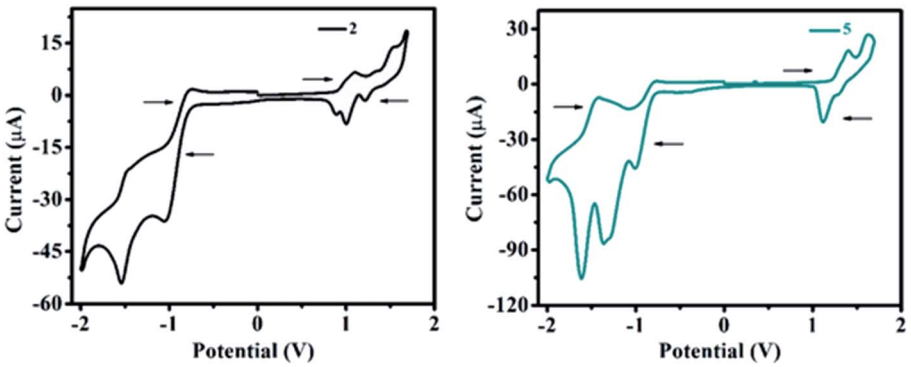

Fig. 11 Cyclic voltammograms (full scan) of **2** and **5**.

Table 3 Electrochemical data of **1–10**

Dye	$E_{oxi}^{peak a}$	$E_{red}^{peak b}$	HOMO[c]	LUMO[d]	$E_g^{EC e}$
1	—	−1.02, −1.33	−6.67[f]	−3.66	3.01
2	1.10, 1.33, 1.52	−1.05, −1.53	−5.63	−3.66	1.97
3	1.15, 1.52	−1.05, −1.52	−5.72	−3.65	2.07
4	0.79, 1.01, 1.49	−1.05, −1.65	−5.34	−3.67	1.67
5	1.30, 1.40, 1.62	−1.00, −1.36, −1.61	−5.87	−3.70	2.17
6	1.14, 1.62	−1.06, −1.45, −1.72	−5.72	−3.63	2.09
7	1.41, 1.62	−1.10, −1.34	−5.97	−3.61	2.36
8	0.82, 0.98, 1.58	−1.04, −1.32	−5.41	−3.65	1.76
9	0.79, 0.95, 1.51	−1.03, −1.73	−5.35	−3.66	1.69
10	1.03, 1.37, 1.58	−1.02, −1.63	−5.62	−3.67	1.95

[a] E_{oxi}^{peak} oxidation peak potential (V). [b] E_{red}^{peak} reduction peak potential (V). [c] HOMO energy level calculated from $E_{HOMO} = -[E_{oxi}^{peak} - E_{redox}\,(Fc/Fc^{+}) + 5.1]$ eV. [d] LUMO energy level calculated from $E_{LUMO} = -[E_{red}^{peak} - E_{redox}\,(Fc/Fc^{+}) + 5.1]$ eV. [e] E_g^{EC} calculated from E_g^{EC} = [HOMO − LUMO] eV. [f] HOMO energy of **1** calculated from HOMO (eV) = $-(E_g^{opt}$ − LUMO) eV (HOMO = −[3.01 − (−3.66)] eV = −6.67 eV).

Further, the oxidation potential was found strongly dependent on the donation tendency of the donor group, consequently, the oxidation potentials of **2–10** decrease with increasing donor strength as **4** ≈ **9** > **8** > **10** > **2** > **6** > **3** > **5** > **7** (Table 3). Lower oxidation peak potentials witnessed for molecules **4**, **8**, **9** (Table 3) are attributed to the presence of the electron-rich –OCH_3 group on the diarylamine moiety in **4** and propensity of phenoxazine (in **8**) and phenothiazine (in **9**) to exhibit larger charge separation with the pyrido-pyrazine acceptor segment (ESI Fig. S54 (below), S55 (above)†) by the formation of stable radical cations and anions, leading to a strong donating effect with lower oxidation potentials as explained by the PET process.[19] However, rigid (cyclic) CBZ substituent on **7** leads to higher oxidation potential than other derivatives (Table 3), which signifies weak donating strength of CBZ amine.

On the other hand, two quasi-reversible waves were observed for **1–10** on the cathodic sweep (Fig. 11 and ESI Fig. S19†) corresponding to the reduction of pyrido[2,3-*b*]pyrazine segment. The extra reduction potential observed for **5** and **6** may be due to the reduction of the electron-withdrawing –NO_2 group (in **5**) and –N=N– group (in **6**) (Table 3).

In order to monitor interfacial charge transport kinetics of materials in optoelectronic devices, the highest occupied and lowest unoccupied molecular orbitals (HOMO and LUMO) of **2–10** were calculated from the first oxidation and reduction potentials obtained in a cyclic voltammogram. Calculated HOMO (−5.34 to −5.97 eV) and LUMO (−3.61 to −3.70 eV) energy levels (Table 3) of **2–10** were found comparable with the reported ambipolar materials.[31] Ambipolar propensity of **2–10** with low band gap (1.67 eV to 2.36 eV) signify the injection of both holes and electron transporting characteristics within a molecule. Further, the HOMO–LUMO energy value and corresponding band gap were found to be altered in accordance with their substituted donor group (Table 3). As a result, compound **4** exhibits a lower band gap (1.67 eV) than other derivatives indicating the influence of a strong electron-donating group (–OCH_3) on a diarylamine moiety (Table 3). Whereas, the CBZ substituted derivative **7** shows a higher band gap (2.36 eV) than other molecules due to the weak electron-donating nature of rigid carbazole (Table 3). Thus, lower band gap and balanced dual charge transport properties of **2–10** make them promising ambipolar materials for organic electronics.

Thermal properties

In order to improve the device performance, good thermal stability and high decomposition temperatures (above 80 °C) are required.[32] The thermogravimetric analysis (TGA) of **2–10** was carried out at the temperature range of 30–1000 °C with a constant heating rate of 10 °C min^{-1} under inert (nitrogen) gas conditions and a melting point of **2–10** were determined by the open capillary method. Thermograms of **2–10** are displayed in Fig. 12 (right), revealing the high thermal stability of materials with no weight loss at low temperatures. Correspondingly, for **2–10**, weight losses between 5% and 10% were found in the range of 140–350 °C and 250–460 °C, respectively. The order of thermal stability of **2–10** is **8** (350 (460)) > **5** (350 (405)) > **6** (350 (378)) > **3** (260 (320)) > **10** (250 (285)) > **7** (240 (440)) > **4** (220 (250)) > **2** (180 (260)) > **9** (140 (260)) (paranthesis: 5(10)% decomposition temperature). Thus, high thermal stabilities and decomposition temperatures of **2–10** reveal prospective usage in organic electronics.

Theoretical investigation

The density functional theory (DFT) and time-dependent DFT (TDDFT) simulations of **1–10** were performed in order to

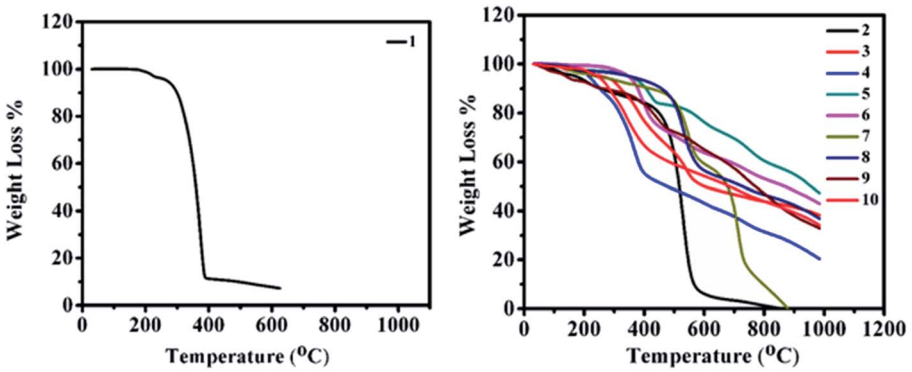

Fig. 12 Thermogravimetric plot of **1** (left) and **2–10** (right).

investigate the relationship between geometrical structure and optoelectronic properties of the dyes. The ground state (S_0) and excited state (S_1 and T_1) geometries of these emitters were optimized with Gaussian 03 software at the B3LYP/6-311++g** level and detailed parameters (the dihedral/bond angle and bond length) are listed in ESI Table S11–S20.† The estimated bond lengths for S_0, S_1 and T_1 geometries of dyes **2–10** were found lower compared to molecule **1**, suggesting push–pull interaction (ESI Tables S11–S20†) (Fig. 13).

While changing the donor in **2–10**, a slight variation in bond lengths was observed (ESI Tables S12–S20†). Moreover, the dihedral angle between D and A (pyrido[2,3-*b*]pyrazine) from S_0 geometries of **2–10** were found in the range of 30°–80° and the bond angle in between pyrido[2,3-*b*]pyrazine acceptor was ~120° suggesting twisted molecular conformation of dyes (ESI Tables S12–S20†). Further significantly altered dihedral angle with different donor moieties is evident, recommending a difference in twisting pattern between D–A structure of **2–10**. The comparative variation in S_0 geometrical parameters of dyes **2** and **7** is marked on its optimized structure and shown in Fig. 14. Besides, compared to S_0 geometries of **2–10**, the structures at S_1 and T_1 experienced significant changes as referred by larger $\Delta(S_1–S_0)/\Delta(T_1–S_0)$ dihedral angles (ESI Tables S12–S20†).

Further, the exploration of molecular orbitals (HOMO and LUMO) distribution are important factors towards computing ΔE_{ST} and designing effective TADF materials.[3] Consequently, molecular orbitals distribution on the optimized structures at S_0, S_1 and T_1 state (Fig. 14, ESI Fig S51–S55†) and the singlet (E_{S1}), triplet (E_{T1}) energies with corresponding ΔE_{ST} (Table 4) for **1–10** were evaluated by the B3LYP/6–311++g** basis set. The positive and negative wave function distribution on HOMO/LUMO orbitals is represented by red and blue colours, respectively. At S_0, the state molecule **1** shows HOMO fully residing all over the moiety and LUMO on pyrido[2,3-*b*]pyrazine acceptor and partial on phenyl ring leading to larger ΔE_{ST} = 0.48 eV (Table 4) due to maximum HOMO–LUMO orbitals overlap (ESI Fig. S51†). While in the case of dyes **2–10**, large dihedral angles between the various donor and pyrido[2,3-*b*]pyrazine planes causes separated HOMO and LUMO electron cloud distributions (ESI Fig S51–S55†) which contributes to achieving a reduced ΔE_{ST} (0.01–0.23 eV) value compared to **1** (Table 4).

HOMO in **2**, **3**, **8** and **9** are mainly localized on its donor diphenylamine (4, 4′ position), naphthylphenylamine (4, 4′ position), phenoxazine (4′ position), phenothiazine (4′ position) respectively and slightly extended to phenyl bridge (ESI Fig. S51, S52, S54 and S55†). While their LUMO is confined on pyrido[2,3-

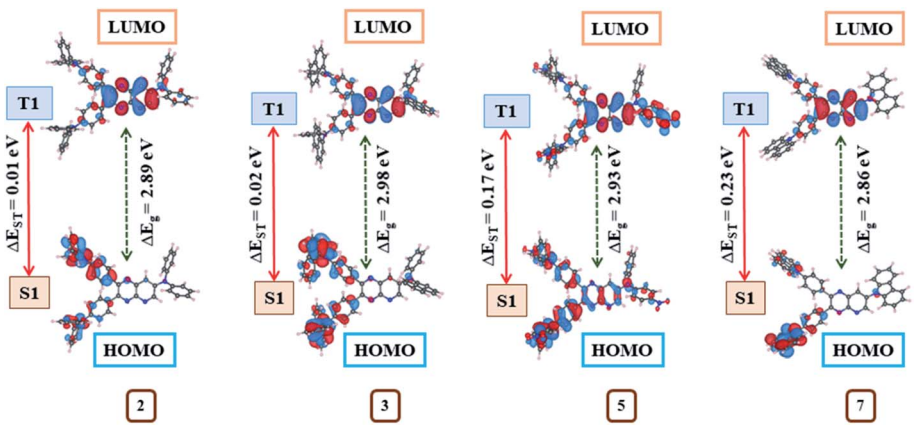

Fig. 13 Correlation diagram showing the ground state (S_0) HOMO and LUMO molecular orbital distribution, the energy gap, and the difference in singlet-triplet excitation energies (ΔE_{ST}) of **2**, **3**, **5** and **7** computed at the B3LYP/6-311++g** level.

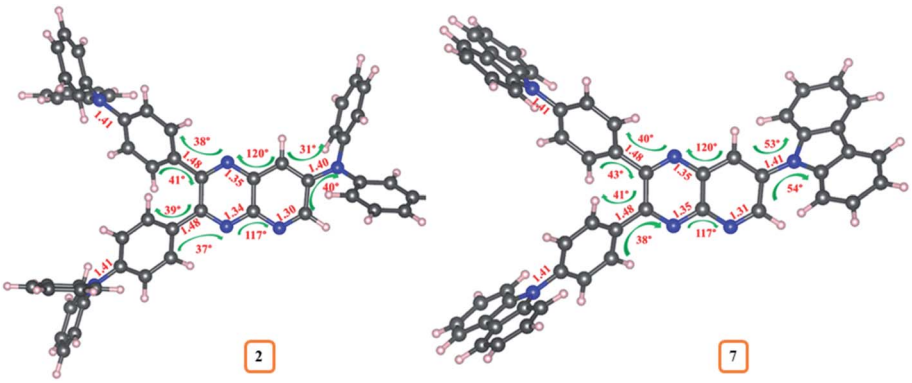

Fig. 14 Variation of geometrical parameters in the optimized geometries of **2** and **7**.

b]pyrazine acceptor and partial on the phenyl bridge (ESI Fig. S51, S52, S54 and S55†). The observed less overlapping between HOMO and LUMO wave function for these dyes is consistent with the principle that the ΔE_{ST} value of a molecule decreases as the overlap diminishes.[3] Consequently, very less ΔE_{ST} values (0.01, 0.02, 0.01, 0.02 eV) were estimated for these dyes (Table 4).

In the case of **4**, HOMO resides on the 4, 4′ position of the donor extended to the phenyl bridge and pyrido[2,3-*b*]pyrazine planes as well as partially on the 7th position of the donor. Besides LUMO is mainly confined to pyrido[2,3-*b*]pyrazine acceptor and partial on phenyl ring (ESI Fig. S52†). Subsequently, dye **4** shows slightly greater overlapping and larger ΔE_{ST} (0.11 eV) (Table 4). Similarly, observed higher HOMO/LUMO orbital overlap is the cause of larger ΔE_{ST} in **5** (0.17 eV) **6** (0.12 eV) and **7** (0.23 eV) (Table 4, ESI Fig. S53 and S54†). Also, the computed ΔE_{ST} value for dye **7** (0.23 eV) and **8** (0.01 eV) are comparable to reported experimental values (0.39 and 0.09 eV, respectively).[8d] Further the electron cloud on HOMO in dye **10** is confined on donor morpholine (4, 4′ position), extending to the phenyl bridge and pyrido[2,3-*b*]pyrazine planes while its LUMO is again on acceptor and partial on phenyl ring (ESI Fig. S55†). As a result, it shows moderate overlapping compared to other dyes and as expected from the orbital distributions, ΔE_{ST} was found at 0.07 eV (Table 4).

In addition, no direct overlap between the highest occupied and lowest unoccupied natural transition orbitals at S_1 and T_1 state designate dominant excited state CT property (Fig. 14, ESI Fig S51–S55†) and lower ΔE_{ST} values (0.01–0.23 eV) (Table 4) in **2–10**.[3] Further, CT absorption and other transitions of **2–10**, were evaluated by simulated absorption spectra in various solvents and gas phases using the TDDFT method (Fig. 15, ESI Fig. S40(b–e)†).

The absorption wavelengths, oscillator strength (*f*) and the vertical electronic transitions of **1–10** in gas and in various solvents are given in ESI Tables S1–S10.† As desired, among various types of transition possesses by dyes **2–10**, the long-wavelength (λ_{max}) transitions originated from HOMO → LUMO or HOMO −2 → LUMO transitions (ESI Tables S2–S10†), and it is often referred to as the CT transition.[33] This CT transition is clear evidence for the presence of D–A architecture in **2–10**.[33]

Further, simulated absorption spectra of **2–10** (Fig. 15(a), ESI Fig. S40(b–e), Tables S2–S10†) on increasing the polarity of solvent (toluene to DMSO) also show variation in the absorption λ_{max} (Table 4) analogous to experimental data (Table 1, Fig. 2, ESI Fig. S4†), suggesting dipole moment changes in the electronic ground-state by the solvent.[15] While self-interaction error in TDDFT arising from the electron transfer in CT state are the

Table 4 Computed absorption wavelength in various solvents, electron affinities, ionization potentials, HOMO–LUMO orbital energies and dipole moments (μ_g), and singlet (E_{S1}) and triplet energy (E_{T1}) levels of **1–10**

	λ_{max} (nm)													
Dye	Toluene	THF	CHL	DCM	DMSO	E_a (eV)	I_p (eV)	E_{HOMO} (eV)	E_{LUMO} (eV)	E_g (eV)	μ_g (Debye)	E_{S1} (eV)	E_{T1} (eV)	ΔE_{ST} (eV)
1	388.9	394.0	392.4	394.5	396.7	1.64	7.91	−6.70	−3.00	3.70	1.52	23.93	23.45	0.48
2	517.2	534.0	528.8	535.6	542.9	1.15	6.03	−5.16	−2.27	2.89	2.65	6.67	6.66	0.01
3	503.0	519.9	514.5	521.5	529.1	1.13	6.01	−5.17	−2.19	2.98	2.16	7.94	7.92	0.02
4	544.7	568.0	560.6	570.3	580.8	0.84	5.64	−4.81	−2.02	2.79	3.53	8.64	8.53	0.11
5	505.8	523.8	517.9	525.7	534.5	2.16	6.81	−5.98	−3.05	2.93	6.28	8.50	8.33	0.17
6	541.3	555.3	551.0	556.7	562.8	1.90	6.09	−5.35	−2.63	2.72	3.11	9.56	9.44	0.12
7	497.2	496.1	496.6	495.9	494.9	1.68	6.59	−5.74	−2.88	2.86	1.84	6.88	6.65	0.23
8	700.7	686.4	691.4	684.8	676.9	1.83	6.05	−5.14	−3.05	2.09	1.58	7.28	7.27	0.01
9	597.2	590.8	593.1	589.9	585.9	1.81	6.24	−5.34	−3.02	2.32	2.64	7.59	7.57	0.02
10	457.9	473.6	468.6	475.1	482.3	0.88	6.49	−5.40	−2.15	3.25	2.05	4.85	4.78	0.07

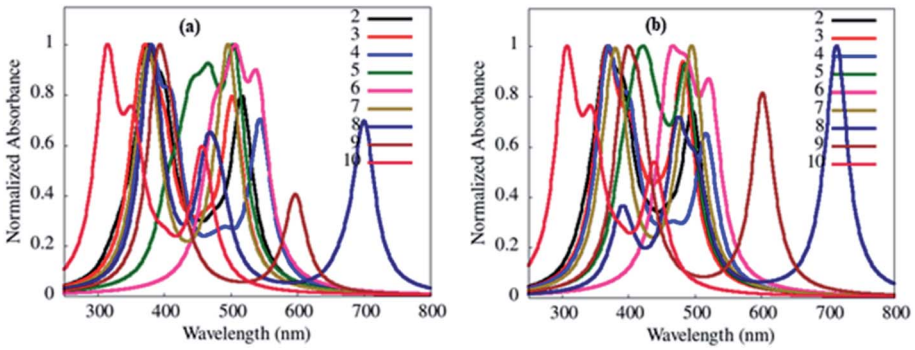

Fig. 15 Simulated absorption transition spectra of **2–10** in toluene (a) and gas phase (b) obtained from the B3LYP/6-311++g** basis set.

causes of red-shifted theoretical absorption transitions than the experimental one.[34]

The computed HOMO and LUMO energy values for **2–10** are −4.81 to −5.98 eV and −2.02 to −3.05 eV, respectively (Table 4). In the dyes **2–10**, C–N coupling between donor amines and acceptor helps to suppress HOMO–LUMO gaps (E_g) (2.09 to 3.25 eV) compared to **1** (3.70 eV) (Table 4). Moreover computed low band gap in **2–10** (Table 4) indicate good hole and electron transporting nature. While observed deviation in experimental and theoretical HOMO–LUMO energies and band gap most likely designate self-interaction error in the orbital energies from the ground-state DFT calculation and or the role of solvent interaction with the molecules.[34]

Besides, IP and EA values shown in Table 4 were estimated by the differences in the total energies of the neutral and cationic/anionic species, respectively. The lowest IP and EA values estimated for **4** in comparison to other compounds reveals strong donating capability due to the presence of $-OCH_3$ group present on the diphenylamine donor segment (Table 4). While higher IP and EA values were obtained for molecule **5** than those for other dyes indicating strong accepting capability due to the presence of the $-NO_2$ group present on the diphenylamine donor segment (Table 4). Small ground state dipole moment exhibited by all dye (except **5**) implies that the dipole vectors cancel one another out due to their opposite directions. The large dipole moment obtained for **5** (6.28) (Table 4) was due to the presence of the polar $-NO_2$ substituent on diphenylamine. The Cartesian coordinates of optimized structures, Mulliken and Lowdin charges of **1–10** are given in ESI Tables S21–S30.†

Conclusion

D–A–D structured pyrido[2,3-*b*]pyrazine amines (**2–10**) were synthesized by the Buchwald–Hartwig amination reaction and investigated for the effect of peripheral amines on their opto-electrochemical and theoretical properties. C–N coupling in dyes offers significant charge transfer (ICT) property and established D–A building in **2–10**. Dyes emit blue–red emissions in solution and solid-state due to the excited CT state. The emission property of dyes was found sensitive towards solvent media used and shows positive solvatochromism. Dyes **2**, **3**, **4**, **5** and **7** possess AIE characteristics and hence could be used as solid-state emissive materials in organic electronics. Dyes **2–10** show the formation of nanoparticles at high f_w in the THF/H_2O mixture as confirmed from DLS and FEG-SEM. In addition, the C–N linkage in dyes controls the oxidation potential, which leads to a reduction in HOMO–LUMO energy band gaps (1.67 to 2.36 eV) and the energy values are comparable with reported ambipolar materials. The thermal stabilities of dyes are found good. Further, the DFT/TDDFT method helps to understand: (i) the extent of push–pull (D–A) interaction in the dyes (ii) degree of twisting on the basis of the dihedral angle between all the aromatic rings in the dyes (iii) tuning of the optoelectrochemical properties was based on the relative strength of donor (iv) correlation of distribution of electron cloud depended on HOMO and LUMO orbital and ΔE_{ST}. Computed small ΔE_{ST} revealed possible TADF characteristics of dyes. Thus, experimental and theoretical results indicate that these molecules have the potential to be used in various optoelectronic applications.

Experimental section

Chemicals and materials

Sigma Aldrich and Alfa Aesar were the commercial sources of all materials and reagents used. HPLC and spectroscopic grade organic solvents were dried using standard procedures and handled in a moisture-free atmosphere. SD fine silica gel (60–120 mesh) with eluent *n*-hexane and chloroform were used for the column chromatography experiment. The progress of reactions and purity of the compounds were checked using thin-layer chromatography (TLC) on silica gel coated glass plates, visualized using UV light (365 nm) and an iodine chamber.

Instrumentation and methods

UV-visible spectra of all compounds were recorded in 10^{-5} mol L^{-1} solutions in a 1 cm path length quartz cuvette and a solid film on a SHIMADZU UV-2401PC at room temperature. The solid films of **2–10** were prepared on quartz glass plate substrate using a spin coater (Holmarc HO-TH-05) at 1000 rpm for 2 min with approximately 6 mg mL^{-1} of sample in chloroform solvent. The emission spectra were measured using a SHIMADZU RF-5301PC fluorescence spectrophotometer. The fluorescence quantum yields of dyes **2–10** were calculated using

quinine sulfate ($\phi_f = 0.54$ in 0.5 M H_2SO_4). AIE study was conducted using 10^{-5} mol L^{-1} THF/H_2O solutions with different percentages of water fractions using a similar UV-visible and fluorescence spectrophotometer. Hydrodynamic particle sizes were obtained from DLS analysis using a Zetasizer (7.12)-MAL1180779. The exact nanoparticles size and morphology of dye 7 were determined by FEG-SEM analysis using the JSM-7600F instrument. Cyclic voltammetry (CV) studies were carried out on a computer-controlled PalmSens3 potentiostat or galvanostat instrument. The CV measurement was carried out with a scan rate of 100 mV s^{-1} at room temperature in anhydrous dichloromethane (DCM) solution using tetrabutylammonium hexafluorophosphate (TBHP) (0.1 M) as a supporting electrolyte. The cell assembly was set up with a three-electrode system as non–aqueous Ag/AgCl (reference) electrode, platinum (Pt) wire (counter electrode) and carbon glassy (working) electrode. The potential of the Ag/AgCl reference electrode was calibrated using the ferrocene/ferrocenium redox couple with the known oxidation potential of +5.1 eV. The thermogravimetric analysis (TGA) was performed using a Metler Toledo instrument (TG) under nitrogen atmosphere. ^{1}H and ^{13}C NMR spectra were recorded using $CDCl_3$ on a Varian UltraShield spectrometer with tetramethylsilane (TMS) as an internal reference at a working frequency of 400 MHz and 100 MHz, respectively. Fourier transform infrared (FT-IR) spectra were recorded using solid powder samples on a PerkinElmer Frontier 91579. Mass spectrometric measurements were recorded using MALDI-TOF (Bruker) and elemental analysis was performed on an EA Euro-elemental analysis instrument. Melting points were recorded in silicon oil bath using the ANALAB melting point apparatus.

Synthetic procedures

Synthetic procedure for 7-bromo-2,3-bis(4-bromophenyl) pyrido[2,3-*b*]pyrazine (1). A mixture of 4,4′-dibromobenzil (1.5 g, 1 mmol) and 5-bromo-2,3-diaminopyridine (0.77 g, 4.07 mmol) was refluxed for 3 hours in 10 mL glacial acetic acid. Afterwards, the reaction mixture was added dropwise in cold distilled water to obtain crude solid and then purified by column chromatography.

Light yellow solid, eluent *n*-hexane : chloroform: 40 : 60, yield: 2.00 g (93%), m. p.: 190 °C, FT-IR (solid, ν_{max}/cm^{-1}): 3030, 2922 (Ar. =C–H str), 1585, 1486 (Ar. –C=C str), 1325 (C–N str), 1062 (Ar. –C–H bend), 817 (C–Br); ^{1}H NMR (400 MHz, $CDCl_3$): δ (ppm) = 9.17 (s, 1H, ArH), 8.65 (d, 1H, ArH, J = 2.4 Hz), 7.55–7.41 (m, 8H, ArH), 7.26 (s, 1H, ArH (1H due to residual $CHCl_3$ in $CDCl_3$)). MALDI-TOF: mass calcd for $C_{19}H_{10}Br_3N_3$ [M^+]: 520.01, found: 519.60; elemental anal. calcd for $C_{19}H_{10}Br_3N_3$: C 43.88, H 1.94, N 8.08%, found: C 43.84, H 2.02, N 8.00%.

General synthetic procedure for 2–10

A mixture of compound **1** (0.2 g, 0.385 mmol) and various diarylamine/heterocyclic amines (1.3 mmol) were dissolved in anhydrous toluene (30 mL) with catalyst $Pd_2(dba)_3$ (20 mg, 0.02 mmol), reagent SPhos (20 mg, 0.04 mmol) and base *t*-BuONa (150 mg, 1.50 mmol). The reaction mixture was heated at 110 °C under the nitrogen atmosphere for 5–12 hours with continuous stirring. The progress of the reaction mixture was continuously monitored through the TLC method. Afterwards, the mixture was cooled to room temperature and extracted with chloroform (3 × 50 mL) followed by water washing (3 × 50 mL). All the organic layers were combined and dried over anhydrous Na_2SO_4 and evaporated to afford the crude product, which was further purified by silica gel column chromatography (eluent : *n*-hexane : chloroform) to obtain yellow-red solids.

4,4′-(7-(Diphenylamino)pyrido[2,3-*b*]pyrazine-2,3-diyl) bis(*N*,*N*-diphenylaniline) (2). Orange solid, eluent *n*-hexane : -chloroform: 30 : 70, yield: 140 mg (46.66%), m. p.: 145 °C. FT-IR (solid, ν_{max}/cm^{-1}): 3034 (Ar. =C–H str), 1585, 1486 (Ar. –C=C str), 1332 (C–N str), 1266, 1165, 1066, 692 (Ar. –C–H bend); ^{1}H NMR (400 MHz, $CDCl_3$): δ (ppm) = 8.92 (s, 1H, ArH), 7.88 (s, 1H, ArH), 7.56–6.99 (m, 39H, ArH) (1H extra due to residual $CHCl_3$ in $CDCl_3$); ^{13}C NMR (100 MHz, $CDCl_3$): δ (ppm) = 154.988, 149.324, 147.737, 147.018, 139.090, 131.386, 130.720, 130.236, 129.794, 125.729, 125.273, 123.662, 122.280, 122.071, 121.414; MALDI-TOF: mass calcd for $C_{55}H_{40}N_6$ [M^+]: 784.95, found: 785.23; elemental anal. calcd for $C_{55}H_{40}N_6$: C 84.16, H 5.14, N 10.71%, found: C 84.23, H 5.10, N 10.65%.

***N*,*N*′-((7-(Naphthalen-1-yl(phenyl)amino)pyrido[2,3-*b*] pyrazine-2,3-diyl)bis(4,1 phenylene))bis(*N*-phenylnaphthalen-1-amine) (3).** Dark orange solid, eluent *n*-hexane : chloroform: 50 : 50, yield: 164 mg (45.68%), m. p.: 155 °C. FT-IR (solid, ν_{max}/cm^{-1}): 3037 (Ar. =C–H str.), 1587, 1493 (Ar. –C=C str), 1357 (C–N str), 1264, 1175, 1072, 772, 694 (Ar. –C–H bend); ^{1}H NMR (400 MHz, $CDCl_3$): δ (ppm) = 9.18 (s, 1H, ArH), 8.99 (s, 1H, ArH), 8.69 (s, 1H, ArH), 7.98–7.80 (m, 29H, ArH), 7.57–7.46 (m, 10H, ArH), 6.85–6.81 (m, 4H, ArH); ^{13}C NMR (100 MHz, $CDCl_3$): δ (ppm) = 156.368, 155.194, 152.548, 149.483, 143.036, 140.873, 134.207, 131.785, 131.567, 129.419, 127.265, 126.794, 124.149, 119.631, 116.512, 116.291, 116.024, 108.866; MALDI-TOF: mass calcd for $C_{67}H_{46}N_6$ [M^+]: 935.12, found: 934.74; elemental anal. calcd for $C_{67}H_{46}N_6$: C 86.05, H 4.96, N 8.99%, found: C 85.99, H 5.05, N 8.93%.

4,4′-(7-(Bis(4-methoxyphenyl)amino)pyrido[2,3-*b*]pyrazine-2,3-diyl)bis(*N*,*N*-bis(4-methoxyphenyl)aniline) (4). Reddish solid, eluent *n*-hexane : chloroform: 20 : 80, yield: 154 mg (41.09%), m. p.: 140 °C. FT-IR (solid, ν_{max}/cm^{-1}): 3057 (Ar. =C–H str), 2920 (Aliph. –C–H str), 1587, 1505, 1440 (Ar. –C=C str), 1348 (C–N str), 1242, 1010, 827 (Ar. –C–H bend); ^{1}H NMR (400 MHz, $CDCl_3$): δ (ppm) = 8.86 (s, 1H, ArH), 8.74 (s, 2H, ArH), 7.57–6.86 (m, 32H, ArH) (1H extra due to residual $CHCl_3$ in $CDCl_3$), 3.86 (s, 18H, ArH, $-OCH_3$); ^{13}C NMR (100 MHz, $CDCl_3$): δ (ppm) = 158.722, 150.717, 143.914, 139.908, 139.202, 132.358, 131.896, 129.554, 127.898, 125.998, 117.513, 116.546, 115.177, 114.697, 55.828; MALDI-TOF: mass calcd for $C_{61}H_{52}N_6O_6$ [M^+]: 965.10, found: 965.09; elemental anal. calcd for $C_{61}H_{52}N_6O_6$: C 75.91, H 5.43, N 8.71%, found: C 75.83, H 5.50, N 8.74%.

4,4′-(7-((4-Nitrophenyl)(phenyl)amino)pyrido[2,3-*b*]pyrazine-2,3-diyl)bis(*N*-(4-nitrophenyl)-*N*-phenylaniline) (5). Orange solid, eluent *n*-hexane : chloroform: 30 : 70, yield: 232 mg (65.72%), m. p.: 212 °C. FT-IR (solid, ν_{max}/cm^{-1}): 3058 (Ar. =C–H str), 1581, 1488 (Ar. –C=C str./–NO_2 str), 1304 (C–N str), 1171, 1108, 836, 749, 692 (Ar. –C–H bend); ^{1}H NMR (400 MHz, $CDCl_3$):

δ (ppm) = 9.03 (s, 1H, ArH), 8.20 (d, 2H, ArH, J = 8.8 Hz), 8.09–8.05 (m, 7H, ArH), 7.67–7.02 (m, 28H, ArH) (1H extra due to residual $CHCl_3$ in $CDCl_3$); ^{13}C NMR (100 MHz, $CDCl_3$): δ (ppm) = 153.807, 152.782, 147.737, 145.508, 143.005, 141.080, 134.067, 131.842, 131.254, 130.625, 128.065, 127.777, 126.782, 126.484, 125.845, 125.190, 121.688, 120.137; MALDI-TOF: mass calcd for $C_{55}H_{37}N_9O_6$ [M^+]: 919.94, found: 920.17; elemental anal. calcd for $C_{55}H_{37}N_9O_6$: C 71.81, H 4.05, N 13.70%, Found C 71.77, H 4.12, N 13.65%.

4,4′-(7-(Phenyl(4-((*E*)-phenyldiazenyl)phenyl)amino)pyrido[2,3-*b*]pyrazine-2,3-diyl)bis(*N*-phenyl-*N*-(4-(phenyldiazenyl)phenyl)aniline) (6). Red solid, eluent *n*-hexane : chloroform: 10 : 90, yield: 192 mg (45.60%), m. p.: 151 °C. FT-IR (solid, ν_{max}/cm^{-1}): 3036 (Ar. =C–H str), 1586, 1489 (Ar. –C=C str), 1334 (C–N str), 1257, 1138, 1063, 686 (Ar. −C–H bend); ^{1}H NMR (400 MHz, $CDCl_3$): δ (ppm) = 9.03 (s, 1H, ArH), 7.91–7.86 (m, 11H, ArH), 7.54–7.11 (m, 40H, ArH); ^{13}C NMR (100 MHz, $CDCl_3$): δ (ppm) = 152.723, 149.771, 149.199, 148.377, 148.214, 147.870, 146.370, 145.353, 141.992, 131.714, 131.433, 131.289, 131.088, 130.968, 130.900, 130.388, 129.734, 129.127, 129.076, 126.274, 126.217, 126.133, 126.065, 124.888, 124.716, 124.373, 124.144, 123.537, 123.158, 123.098, 122.805, 122.612; MALDI-TOF: mass calcd for $C_{73}H_{52}N_{12}$ [M^+]: 1097.27, found: 1097.31; elemental anal. calcd for $C_{73}H_{52}N_{12}$: C 79.91, H 4.78, N 15.32%, found: C 79.82, H 4.88, N 15.27%.

9,9′-((7-(9*H*-Carbazol-9-yl)pyrido[2,3-*b*]pyrazine-2,3-diyl)bis(4,1-phenylene))bis(9*H*-carbazole) (7). Yellow solid, eluent *n*-hexane : chloroform: 50 : 50, yield: 188 mg (62.87%), m. p.: >300 °C. FT-IR (solid, ν_{max}/cm^{-1}): 3051 (Ar. =C–H str), 1593, 1448 (Ar. –C=C str), 1326 (C–N str), 1226, 1161, 745 (Ar. –C–H bend); ^{1}H NMR (400 MHz, $CDCl_3$): δ (ppm) = 9.60 (s, 1H, ArH), 8.85 (s, 1H, ArH), 8.25–8.00 (m, 8H, ArH), 7.77–7.28 (m, 24H, ArH); ^{13}C NMR (100 MHz, $CDCl_3$): δ (ppm) = 155.798, 154.924, 153.425, 140.424, 140.112, 139.511, 137.141, 131.709, 127.115, 126.247, 124.751, 124.139, 122.030, 121.420, 120.848, 109.709; MALDI-TOF: mass calcd for $C_{55}H_{34}N_6$ [M^+]: 778.90, found: 779.21; elemental anal. calcd for $C_{55}H_{34}N_6$: C 84.81, H 4.40, N 10.79%, Found C 84.75, H 4.34, N 10.88%.

10,10′-((7-(10*H*-Phenoxazin-10-yl)pyrido[2,3-*b*]pyrazine-2,3-diyl)bis(4,1-phenylene))bis(10*H*-phenoxazine) (8). Dark red solid, eluent *n*-hexane : chloroform: 40 : 60, yield: 244 mg (76.97%), m. p.: 202 °C. FT-IR (solid, ν_{max}/cm^{-1}): 3054 (Ar. =C–H str), 1591, 1482 (Ar. –C=C str), 1334 (C–N str), 1267, 1032, 735, 620 (Ar. –C–H bend); ^{1}H NMR (400 MHz, $CDCl_3$): δ (ppm) = 9.26 (s, 1H, ArH), 8.70 (s, 1H, ArH), 7.91 (dd, 7H, ArH, J = 8 Hz), 6.86–6.56 (m, 25H, ArH); ^{13}C NMR (100 MHz, $CDCl_3$): δ (ppm) = 157.491, 156.283, 144.587, 143.970, 133.779, 132.973, 132.638, 131.190, 130.949, 123.559, 123.454, 123.414, 123.319, 123.141, 121.780, 116.420, 115.699, 113.913, 113.263, 113.136; MALDI-TOF: mass calcd for $C_{55}H_{34}N_6O_3$ [M^+]: 826.90, found: 827.23; elemental anal. calcd for $C_{55}H_{34}N_6O_3$: C 79.89, H 4.14, N 10.16%, found: C 79.80, H 4.20, N 10.21%.

10,10′-((7-(10*H*-Phenothiazin-10-yl)pyrido[2,3-*b*]pyrazine-2,3-diyl)bis(4,1-phenylene))bis(10*H*-phenothiazine) (9). Orange solid, eluent *n*-hexane : chloroform: 10 : 90, yield: 191 mg (56.67%), m. p.: 170 °C. FT-IR (solid, ν_{max}/cm^{-1}): 3056 (Ar. =C–H str), 1582, 1458 (Ar. –C=C str), 1342 (C–N str), 1231, 1168, 829, 739 (Ar. –C–H bend); ^{1}H NMR (400 MHz, $CDCl_3$): δ (ppm) = 9.05 (s, 1H, ArH), 8.12–8.00 (m, 1H, ArH), 7.55–7.28 (m, 33H, ArH (1H extra due to residual $CHCl_3$ in $CDCl_3$)); ^{13}C NMR (100 MHz, $CDCl_3$): δ (ppm) = 152.803, 150.086, 143.695, 140.976, 133.797, 133.695, 132.588, 132.121, 131.848, 131.457, 129.614, 127.109, 123.621, 116.184, 111.883, 109.831; MALDI-TOF: mass calcd for $C_{55}H_{34}N_6S_3$ [M^+]: 875.09, found: 875.19; elemental anal. calcd for $C_{55}H_{34}N_6S_3$: C 75.49, H 3.92, N 9.60%, found: C 75.55, H 3.88, N 9.66%.

4,4′-((7-Morpholinopyrido[2,3-*b*]pyrazine-2,3-diyl)bis(4,1-phenylene))dimorpholine (10). Dark orange solid, eluent-chloroform, yield: 201 mg (97.57%), m. p.: 142 °C. FT-IR (solid, ν_{max}/cm^{-1}): 3049 (Ar. =C–H str), 2848 (Aliph. –C–H str), 1595, 1447 (Ar. –C=C str), 1372 (C–N str), 1233, 1110, 925, 825, 597 (Ar. –C–H bend); ^{1}H NMR (400 MHz, $CDCl_3$): δ (ppm) = 8.97 (d, 1H, ArH, J = 2.4 Hz), 7.64–7.28 (m, 9H, ArH (1H extra due to residual $CHCl_3$ in $CDCl_3$)), 6.61 (d, 1H, ArH, J = 8.4 Hz), 3.94 (t, 12H, ArH, J = 4.4 Hz), 3.42 (t, 4H, $-CH_2$, J = 4.3 Hz), 3.26 (t, 8H, $-CH_2$, J = 4.5 Hz); ^{13}C NMR (100 MHz, $CDCl_3$): δ (ppm) = 158.109, 150.246, 147.480, 132.899, 131.541, 130.878, 129.455, 116.750, 115.820, 103.591, 66.560, 48.280; MALDI-TOF: mass calcd for $C_{31}H_{34}N_6O_3$ [M^+]: 538.64, found: 539.06; elemental anal. calcd for $C_{31}H_{34}N_6O_3$: C 69.12, H 6.36, N 15.60%, found: C 69.04, H 6.42, N 15.65%.

Preparation of nanoaggregates/nanoparticles. The reported procedure used for formation of organic nanoparticles in a mixture of good (*e.g.* THF) and poor (*e.g.* H_2O) solvents.[35] In a 5 mL volumetric flask, aliquots of 10^{-4} M stock THF solutions were transferred. Further, series of 10^{-5} M solutions were prepared by varying percentages of water content (0–90 vol%) in the appropriate amount of added THF solvent. The photophysical measurements of the resultant solutions were then performed immediately.

Theoretical section. DFT and time-dependant density functional theoretical (TD-DFT) calculations on the molecules **1–10** were performed using the Gaussian 03 software package.[36] The geometry of the ground state structure was determined by using B3LYP[37,38] as exchange–correlation functional (XC) and the 6–311++g** basis set. Further, to assess the structures were indeed in the ground state, the frequency calculations were performed using the same XC and basis set. UV-VIS spectra were calculated in the gas phase *via* TD-DFT. A Polarizable Continuum Model (PCM)[39] was used to include the effects of solvents–toluene, dichloromethane, chloroform, tetrahydrofuran, and dimethylsulphoxide. Using HOMO–LUMO, the intramolecular charge distribution was determined and visualized using VESTA;[40] red represents positive, and blue represents negative. 1/10 of the maximum value of the isosurface is the iso value for all the molecules. Partial atomic charges on the atoms were estimated using Mulliken[41] and Lowdin[42] charge analysis. ΔE_{ST} was calculated as $E_{S1} - E_{T1}$, where E_{S1} and E_{T1} are the energies of the lowest singlet (S_1) and lowest triplet (T_1) excited state, respectively. The energies are obtained by optimizing the structures in excited states. All the calculations were performed using the same XC and on the above-mentioned set basis, including the calculation of HOMO–LUMO gap, electron-affinity and ionization potential.

Author contributions

Rajesh M. Kamble: conceptualization, investigation, visualization, resources, supervision, writing – review and editing

Deepak M. Kapse and Pooja S. Singh: data curation, investigation, writing – original draft

Mohammed Ghadiyali and Sajeev Chacko: formal/theoretical (computational) analysis

Conflicts of interest

The authors declare no conflict of interest.

Acknowledgements

The authors are greatly thankful to Micro-Analytical Laboratory, Department of Chemistry, University of Mumbai for providing Instrumental facilities, National NMR center and Department of Chemistry, IIRBS Kerala for providing NMR services, TIFR-Mumbai for MALDI-TOF and SAIF-IIT Bombay for FEG-SEM characterization.

References

1 (*a*) M. Madhu, R. Ramakrishnan, V. Vijay and M. Hariharan, *Chem. Rev.*, 2021, **121**, 8234; (*b*) J. Chen, Y. Chen, L.-W. Feng, C. Gu, G. Li, N. Su, G. Wang, S. M. Swick, W. Huang, X. Guo, A. Facchetti and T. J. Marks, *EnergyChem*, 2020, **2**, 100042; (*c*) M. Poddar, G. Sivakumar and R. Misra, *J. Mater. Chem. C*, 2019, **7**, 14798; (*d*) E. Ravindran and N. Somanathan, *J. Mater. Chem. C*, 2017, **5**, 7436.

2 (*a*) J. Mei, Y. Hong, J. W. Y. Lam, A. Qin, Y. Tang and B. Z. Tang, *Adv. Mater.*, 2014, **26**, 5429; (*b*) J. Mei, N. L. C. Leung, R. T. K. Kwok, J. W. Y. Lam and B. Z. Tang, *Chem. Rev.*, 2015, **115**, 11718; (*c*) J. Luo, Z. Xie, J. W. Y. Lam, L. Cheng, H. Chen, C. Qiu, H. S. Kwok, X. Zhan, Y. Liu, D. Zhu and B. Z. Tang, *Chem. Commun.*, 2001, 1740; (*d*) Y. Chen, J. W. Y. Lam, R. T. K. Kwok, B. Liu and B. Z. Tang, *Mater. Horiz.*, 2019, **6**, 428.

3 (*a*) Z. Yang, Z. Mao, Z. Xie, Y. Zhang, S. Liu, J. Zhao, J. Xu, Z. Chi and M. P. Aldred, *Chem. Soc. Rev.*, 2017, **46**, 915; (*b*) T. Huang, W. Jiang and L. Duan, *J. Mater. Chem. C*, 2018, **6**, 5577; (*c*) X. Yin, Y. He, X. Wang, Z. Wu, E. Pang, J. Xu and J. Wang, *Front. Chem.*, 2020, **8**, 725; (*d*) P. S. Singh, P. M. Badani and R. M. Kamble, *J. Photochem. Photobiol., A*, 2021, **419**, 113457; (*e*) P. S. Singh, M. Ghadiyali, S. Chacko and R. M. Kamble, *J. Lumin.*, 2022, **242**, 118568.

4 (*a*) K. Zhou, H. Dong, H. L. Zhang and W. Hu, *Phys. Chem. Chem. Phys.*, 2014, **16**, 22448; (*b*) J. Zaumseil and H. Sirringhaus, *Chem. Rev.*, 2007, **107**, 1296.

5 (*a*) Y. Sakamoto, T. Suzuki, M. Kobayashi, Y. Gao, Y. Fukai, Y. Inoue, F. Sato and S. Tokito, *J. Am. Chem. Soc.*, 2004, **126**, 8138; (*b*) Z. Liang, Q. Tang, J. Xu and Q. Miao, *Adv. Mater.*, 2011, **23**, 1535.

6 (*a*) P. Ledwon, R. Motyka, K. Ivaniuk, A. Pidluzhna, N. Martyniuk, P. Stakhira, G. Baryshnikov, B. F. Minaev and H. Agren, *Dyes Pigm.*, 2020, **173**, 108008; (*b*) P. S. Singh, S. Chacko and R. M. Kamble, *New J. Chem.*, 2019, **43**, 6973; (*c*) D. N. Kanekar, S. Chacko and R. M. Kamble, *Dyes Pigm.*, 2019, **167**, 36–50; (*d*) S. S. Mahadik, D. R. Garud, R. V. Pinjari and R. M. Kamble, *J. Mol. Struct.*, 2022, **1248**, 131541.

7 (*a*) D. Dong, D. Fang, H. Li, C. Zhu, X. Zhao, J. Li, L. Jin, L. Xie, L. Chen, J. Zhao, H. Zhang and W. Huang, *Chem.–Asian J.*, 2017, **12**, 920; (*b*) P. S. Singh, P. M. Badani and R. M. Kamble, *New J. Chem.*, 2019, **43**, 19379.

8 (*a*) H. Zhao, Y. Wei, J. Zhao and M. Wang, *Dyes Pigm.*, 2009, **81**, 245; (*b*) T. Huang, D. Liu, J. Jiang and W. Jiang, *Chem. - Eur. J.*, 2019, **25**, 10926; (*c*) S. S. Mahadik, D. R. Garud, A. P. Ware, S. S. Pingale and R. M. Kamble, *Dyes Pigm.*, 2021, **184**, 108742; (*d*) B. Sk, S. Sharma, A. James, S. Kundu and A. Patra, *J. Mater. Chem. C*, 2020, **8**, 12943.

9 (*a*) Z. Zheng, Q. Dong, L. Gou, J.-H. Su and J. Huang, *J. Mater. Chem. C*, 2014, **2**, 9858; (*b*) D. N. Kanekar, S. Chacko and R. M. Kamble, *New J. Chem.*, 2020, **44**, 3278.

10 (*a*) P. Agarwala and D. Kabra, *J. Mater. Chem. A*, 2017, **5**, 1348; (*b*) F. Baraket, B. Pedras, E. Torres, M. J. Brites, M. Dammak and M. N. Berberan-Santos, *Dyes Pigm.*, 2020, **175**, 108114; (*c*) P. Ledwon, *Org. Electron.*, 2019, **75**, 105422.

11 (*a*) A. S. Guran and S. L. Buchwald, *J. Am. Chem. Soc.*, 1994, **116**, 7901; (*b*) F. Paul, J. Patt and J. F. Hartwig, *J. Am. Chem. Soc.*, 1994, **116**, 5969.

12 S. Xue, W. Liu, X. Qiu, Y. Gao and W. Yang, *J. Phys. Chem. C*, 2014, **118**, 18668.

13 S. A. Jenekhe, L. Lu and M. M. Alam, *Macromolecules*, 2001, **34**, 7315.

14 L. Zhao, X. Ren and X. Yan, *CCS Chem.*, 2021, **3**, 678.

15 J. R. Lakowicz, *Principles of Fluorescence Spectroscopy*, University of Maryland School of Medicine Baltimore, Maryland, USA, 3rd edn, 2006.

16 K. M. Franziska and J. J. M. Thomas, *Sci. China Chem.*, 2018, **61**, 909.

17 L. Xue, Y. Pan, S. Zhang, Y. Chen, H. Yu, Y. Yang, L. Mo, Z. Sun, L. Li and H. Yang, *Crystals*, 2021, **11**, 840.

18 Z. Ning, Z. Chen, Q. Zhang, Y. Yan, S. Qian, Y. Cao and H. Tian, *Adv. Funct. Mater.*, 2007, **17**, 3799.

19 (*a*) J. Daub, R. Engl, J. Kurzawa, S. E. Miller, S. Schneider, A. Stockmann and M. R. Wasielewski, *J. Phys. Chem. A*, 2001, **105**, 5655; (*b*) A. P. Kulkarni, P. Wu, T. W. Kwon and S. A. Jenekhe, *J. Phys. Chem. B*, 2005, **109**, 19584; (*c*) D. W. Cho, M. Fujitsuka, A. Sugimoto, U. C. Yoon, P. S. Mariano and T. Majima, *J. Phys. Chem. B*, 2006, **110**, 11062.

20 (*a*) C. Reichardt, *Angew. Chem., Int. Ed. Engl.*, 1979, **18**, 98; (*b*) C. Reichardt, *Chem. Rev.*, 1994, **94**, 2319.

21 A. Weller, *Angew. Phys. Chem.*, 1956, **60**, 1144.

22 W. Rettig, *Angew. Chem., Int. Ed. Engl.*, 1986, **25**, 971.

23 E. Lippert, *Z. Elektrochem.*, 1957, **61**, 962.

24 E. G. McRae, *J. Phys. Chem.*, 1957, **61**, 562.

25 N. G. Bakhshiev, *Opt. Spectrosc.*, 1962, **13**, 24.

26 R. P. Paitandi, R. S. Singh, B. K. Dwivedi, V. D. Singh and D. S. Pandey, *Dalton Trans.*, 2018, **47**, 3785.

27 Z. J. Ning, Y. C. Zhou, Q. Zhang, D. G. Ma, J. J. Zhang and H. Tian, *J. Photochem. Photobiol., A*, 2007, **192**, 8.

28 H. Li, Z. Chi, X. Zhang, B. Xu, S. Liu, Y. Zhang and J. Xu, *Chem. Commun.*, 2011, **47**, 11273.
29 M. Danaei, M. Dehghankhold, S. Ataei, F. H. Davarani, R. Javanmard, A. Dokhani, S. Khorasani and M. R. Mozafari, *Pharmaceutics*, 2018, **10**, 57.
30 J. Shi, N. Chang, C. Li, J. Mei, C. Deng, X. Luo, Z. Liu, Z. Bo, Y. Q. Dong and B. Z. Tang, *Chem. Commun.*, 2012, **48**, 10675.
31 (*a*) H. Xia, D. Liu, X. Xua and Q. Miao, *Chem. Commun.*, 2013, **49**, 4301; (*b*) L. Wang, X. Zhang, H. Tian, Y. Lu, Y. Geng and F. Wang, *Chem. Commun.*, 2013, **49**, 11272.
32 M.-X. Yu, J.-P. Duan, C.-H. Lin, C.-H. Cheng and Y.-T. Tao, *Chem. Mater.*, 2002, **14**, 3958.
33 Y. Zhu, A. P. Kulkani, P.-T. Wu and S. A. Jenekhe, *Chem. Mater.*, 2008, **20**, 4200.
34 A. Elangovan, K.-M. Kao, S.-W. Yang, Y.-L. Chen, T.-I. Ho and Y. O. J. Su, *J. Org. Chem.*, 2005, **70**, 4460.
35 H. Kasai, H. S. Nalwa, H. Oikawa, S. Okada, H. Matsuda, N. Minami, A. Kakuta, K. Ono, A. Mukoh and H. N. H. Nakanishi, *Jpn. J. Appl. Phys.*, 1992, **31**, L1132.
36 M. J. Frisch, G. W. Trucks, H. B. Schlegel, G. E. Scuseria, M. A. Robb, J. R. Cheeseman, J. A. Montgomery Jr, T. Vreven, K. N. Kudin, J. C. Burant, J. M. Millam, S. S. Iyengar, J. Tomasi, V. Barone, B. Mennucci, M. Cossi, G. Scalmani, N. Rega, G. A. Petersson, H. Nakatsuji, M. Hada, M. Ehara, K. Toyota, R. Fukuda, J. Hasegawa, M. Ishida, T. Nakajima, Y. Honda, O. Kitao, H. Nakai, M. Klene, X. Li, J. E. Knox, H. P. Hratchian, J. B. Cross, V. Bakken, C. Adamo, J. Jaramillo, R. Gomperts, R. E. Stratmann, O. Yazyev, A. J. Austin, R. Cammi, C. Pomelli, J. W. Ochterski, P. Y. Ayala, K. Morokuma, G. A. Voth, P. Salvador, J. J. Dannenberg, V. G. Zakrzewski, S. Dapprich, A. D. Daniels, M. C. Strain, O. Farkas, D. K. Malick, A. D. Rabuck, K. Raghavachari, J. B. Foresman, J. V. Ortiz, Q. Cui, A. G. Baboul, S. Clifford, J. Cioslowski, B. B. Stefanov, G. Liu, A. Liashenko, P. Piskorz, I. Komaromi, R. L. Martin, D. J. Fox, T. Keith, M. A. Al-Laham, C. Y. Peng, A. Nanayakkara, M. Challacombe, P. M. W. Gill, B. Johnson, W. Chen, M. W. Wong, C. Gonzalez, and J. A. Pople. *Gaussian 03, Revision C.02*. Gaussian, 2 Inc., Wallingford, CT, 2004.
37 K. Ks and K. D. Jordan, *J. Phys. Chem.*, 1994, **98**, 10089.
38 P. J. Stephens, F. J. Devlin, C. F. Chabalowski, M. J. Frisch and A. b. initio, *J. Phys. Chem.*, 1994, **98**, 11623.
39 H. Ilona, H. Peter and P. Andras, *J. Comput. Chem.*, 2004, **25**, 1522.
40 M. Koichi and I. Fujio, *J. Appl. Crystallogr.*, 2008, **41**, 653.
41 R. S. Mulliken, *J. Chem. Phys.*, 1955, **23**, 1833.
42 P.-O. Lowdin, *J. Chem. Phys.*, 1953, **21**, 374.